

Search for Higgs boson production in oppositely charged dilepton and missing energy events in $p\bar{p}$ collisions at $\sqrt{s} = 1.96$ TeV

V.M. Abazov,³² B. Abbott,⁶⁹ B.S. Acharya,²⁶ M. Adams,⁴⁶ T. Adams,⁴⁴ G.D. Alexeev,³² G. Alkhalaf,³⁶ A. Alton^a,⁵⁸ G. Alverson,⁵⁷ A. Askew,⁴⁴ S. Atkins,⁵⁵ K. Augsten,⁷ C. Avila,⁵ F. Badaud,¹⁰ L. Bagby,⁴⁵ B. Baldin,⁴⁵ D.V. Bandurin,⁴⁴ S. Banerjee,²⁶ E. Barberis,⁵⁷ P. Baringer,⁵³ J.F. Bartlett,⁴⁵ U. Bassler,¹⁵ V. Bazterra,⁴⁶ A. Bean,⁵³ M. Begalli,² L. Bellantoni,⁴⁵ S.B. Beri,²⁴ G. Bernardi,¹⁴ R. Bernhard,¹⁹ I. Bertram,³⁹ M. Besançon,¹⁵ R. Beuselinck,⁴⁰ P.C. Bhat,⁴⁵ S. Bhatia,⁶⁰ V. Bhatnagar,²⁴ G. Blazey,⁴⁷ S. Blessing,⁴⁴ K. Bloom,⁶¹ A. Boehnlein,⁴⁵ D. Boline,⁶⁶ E.E. Boos,³⁴ G. Borissov,³⁹ T. Bose,⁵⁶ A. Brandt,⁷² O. Brandt,²⁰ R. Brock,⁵⁹ A. Bross,⁴⁵ D. Brown,¹⁴ J. Brown,¹⁴ X.B. Bu,⁴⁵ M. Buehler,⁴⁵ V. Buescher,²¹ V. Bunichev,³⁴ S. Burdin^b,³⁹ C.P. Buszello,³⁸ E. Camacho-Pérez,²⁹ B.C.K. Casey,⁴⁵ H. Castilla-Valdez,²⁹ S. Caughron,⁵⁹ S. Chakrabarti,⁶⁶ D. Chakraborty,⁴⁷ K.M. Chan,⁵¹ A. Chandra,⁷⁴ E. Chapon,¹⁵ G. Chen,⁵³ S. Chevalier-Théry,¹⁵ D.K. Cho,⁷¹ S.W. Cho,²⁸ S. Choi,²⁸ B. Choudhary,²⁵ S. Cihangir,⁴⁵ D. Claes,⁶¹ J. Clutter,⁵³ M. Cooke,⁴⁵ W.E. Cooper,⁴⁵ M. Corcoran,⁷⁴ F. Couderc,¹⁵ M.-C. Cousinou,¹² A. Croc,¹⁵ D. Cutts,⁷¹ A. Das,⁴² G. Davies,⁴⁰ S.J. de Jong,^{30,31} E. De La Cruz-Burelo,²⁹ F. Déliot,¹⁵ R. Demina,⁶⁵ D. Denisov,⁴⁵ S.P. Denisov,³⁵ S. Desai,⁴⁵ C. Deterre,¹⁵ K. DeVaughan,⁶¹ H.T. Diehl,⁴⁵ M. Diesburg,⁴⁵ P.F. Ding,⁴¹ A. Dominguez,⁶¹ A. Dubey,²⁵ L.V. Dudko,³⁴ D. Duggan,⁶² A. Duperrin,¹² S. Dutt,²⁴ A. Dyshkant,⁴⁷ M. Eads,⁶¹ D. Edmunds,⁵⁹ J. Ellison,⁴³ V.D. Elvira,⁴⁵ Y. Enari,¹⁴ H. Evans,⁴⁹ A. Evdokimov,⁶⁷ V.N. Evdokimov,³⁵ G. Facini,⁵⁷ A. Fauré,¹⁵ L. Feng,⁴⁷ T. Ferbel,⁶⁵ F. Fiedler,²¹ F. Filthaut,^{30,31} W. Fisher,⁵⁹ H.E. Fisk,⁴⁵ M. Fortner,⁴⁷ H. Fox,³⁹ S. Fuess,⁴⁵ A. Garcia-Bellido,⁶⁵ J.A. García-González,²⁹ G.A. García-Guerra^c,²⁹ V. Gavrilov,³³ P. Gay,¹⁰ W. Geng,^{12,59} D. Gerbaudo,⁶³ C.E. Gerber,⁴⁶ Y. Gershtein,⁶² G. Ginter,^{45,65} G. Golovanov,³² A. Goussiou,⁷⁶ P.D. Grannis,⁶⁶ S. Greder,¹⁶ H. Greenlee,⁴⁵ G. Grenier,¹⁷ Ph. Gris,¹⁰ J.-F. Grivaz,¹³ A. Grohsjean^d,¹⁵ S. Grünendahl,⁴⁵ M.W. Grünewald,²⁷ T. Guillemain,¹³ G. Gutierrez,⁴⁵ P. Gutierrez,⁶⁹ S. Hagopian,⁴⁴ J. Haley,⁵⁷ L. Han,⁴ K. Harder,⁴¹ A. Harel,⁶⁵ J.M. Hauptman,⁵² J. Hays,⁴⁰ T. Head,⁴¹ T. Hebbeker,¹⁸ D. Hedin,⁴⁷ H. Hegab,⁷⁰ A.P. Heinson,⁴³ U. Heintz,⁷¹ C. Hensel,²⁰ I. Heredia-De La Cruz,²⁹ K. Herner,⁵⁸ G. Hesketh^f,⁴¹ M.D. Hildreth,⁵¹ R. Hirosky,⁷⁵ T. Hoang,⁴⁴ J.D. Hobbs,⁶⁶ B. Hoeneisen,⁹ J. Hogan,⁷⁴ M. Hohlfeld,²¹ I. Howley,⁷² Z. Hubacek,^{7,15} V. Hynek,⁷ I. Iashvili,⁶⁴ Y. Ilchenko,⁷³ R. Illingworth,⁴⁵ A.S. Ito,⁴⁵ S. Jabeen,⁷¹ M. Jaffré,¹³ A. Jayasinghe,⁶⁹ M.S. Jeong,²⁸ R. Jesik,⁴⁰ K. Johns,⁴² E. Johnson,⁵⁹ M. Johnson,⁴⁵ A. Jonckheere,⁴⁵ P. Jonsson,⁴⁰ J. Joshi,⁴³ A.W. Jung,⁴⁵ A. Juste,³⁷ K. Kaadze,⁵⁴ E. Kajfasz,¹² D. Karmanov,³⁴ P.A. Kasper,⁴⁵ I. Katsanos,⁶¹ R. Kehoe,⁷³ S. Kermiche,¹² N. Khalatyan,⁴⁵ A. Khanov,⁷⁰ A. Kharchilava,⁶⁴ Y.N. Kharzheev,³² I. Kiselevich,³³ J.M. Kohli,²⁴ A.V. Kozelov,³⁵ J. Kraus,⁶⁰ S. Kulikov,³⁵ A. Kumar,⁶⁴ A. Kupco,⁸ T. Kurča,¹⁷ V.A. Kuzmin,³⁴ S. Lammers,⁴⁹ G. Landsberg,⁷¹ P. Lebrun,¹⁷ H.S. Lee,²⁸ S.W. Lee,⁵² W.M. Lee,⁴⁵ X. Lei,⁴² J. Lellouch,¹⁴ H. Li,¹¹ L. Li,⁴³ Q.Z. Li,⁴⁵ J.K. Lim,²⁸ D. Lincoln,⁴⁵ J. Linnemann,⁵⁹ V.V. Lipaev,³⁵ R. Lipton,⁴⁵ H. Liu,⁷³ Y. Liu,⁴ A. Lobodenko,³⁶ M. Lokajicek,⁸ R. Lopes de Sa,⁶⁶ H.J. Lubatti,⁷⁶ R. Luna-Garcia^g,²⁹ A.L. Lyon,⁴⁵ A.K.A. Maciel,¹ R. Madar,¹⁵ R. Magaña-Villalba,²⁹ S. Malik,⁶¹ V.L. Malyshev,³² Y. Maravin,⁵⁴ J. Martínez-Ortega,²⁹ R. McCarthy,⁶⁶ C.L. McGivern,⁴¹ M.M. Meijer,^{30,31} A. Melnitchouk,⁶⁰ D. Menezes,⁴⁷ P.G. Mercadante,³ M. Merkin,³⁴ A. Meyer,¹⁸ J. Meyer,²⁰ F. Miconi,¹⁶ N.K. Mondal,²⁶ M. Mulhearn,⁷⁵ E. Nagy,¹² M. Naimuddin,²⁵ M. Narain,⁷¹ R. Nayyar,⁴² H.A. Neal,⁵⁸ J.P. Negret,⁵ P. Neustroev,³⁶ T. Nunnemann,²² J. Orduna,⁷⁴ N. Osman,¹² J. Osta,⁵¹ M. Padilla,⁴³ A. Pal,⁷² N. Parashar,⁵⁰ V. Parihar,⁷¹ S.K. Park,²⁸ R. Partridge^e,⁷¹ N. Parua,⁴⁹ A. Patwa,⁶⁷ B. Penning,⁴⁵ M. Perfilov,³⁴ Y. Peters,⁴¹ K. Petridis,⁴¹ G. Petrillo,⁶⁵ P. Pétroff,¹³ M.-A. Pleier,⁶⁷ P.L.M. Podesta-Lerma^h,²⁹ V.M. Podstavkov,⁴⁵ A.V. Popov,³⁵ M. Prewitt,⁷⁴ D. Price,⁴⁹ N. Prokopenko,³⁵ J. Qian,⁵⁸ A. Quadt,²⁰ B. Quinn,⁶⁰ M.S. Rangel,¹ K. Ranjan,²⁵ P.N. Ratoff,³⁹ I. Razumov,³⁵ P. Renkel,⁷³ I. Ripp-Baudot,¹⁶ F. Rizatdinova,⁷⁰ M. Rominsky,⁴⁵ A. Ross,³⁹ C. Royon,¹⁵ P. Rubinov,⁴⁵ R. Ruchti,⁵¹ G. Sajot,¹¹ P. Salcido,⁴⁷ A. Sánchez-Hernández,²⁹ M.P. Sanders,²² A.S. Santosⁱ,¹ G. Savage,⁴⁵ L. Sawyer,⁵⁵ T. Scanlon,⁴⁰ R.D. Schamberger,⁶⁶ Y. Scheglov,³⁶ H. Schellman,⁴⁸ S. Schlobohm,⁷⁶ C. Schwanenberger,⁴¹ R. Schwienhorst,⁵⁹ J. Sekaric,⁵³ H. Severini,⁶⁹ E. Shabalina,²⁰ V. Shary,¹⁵ S. Shaw,⁵⁹ A.A. Shchukin,³⁵ R.K. Shivpuri,²⁵ V. Simak,⁷ P. Skubic,⁶⁹ P. Slattery,⁶⁵ D. Smirnov,⁵¹ K.J. Smith,⁶⁴ G.R. Snow,⁶¹ J. Snow,⁶⁸ S. Snyder,⁶⁷ S. Söldner-Rembold,⁴¹ L. Sonnenschein,¹⁸ K. Soustruznik,⁶ J. Stark,¹¹ D.A. Stoyanova,³⁵ M. Strauss,⁶⁹ L. Suter,⁴¹ P. Svoisky,⁶⁹ M. Takahashi,⁴¹ M. Titov,¹⁵ V.V. Tokmenin,³² Y.-T. Tsai,⁶⁵ K. Tschann-Grimm,⁶⁶ D. Tsybychev,⁶⁶ B. Tuchming,¹⁵ C. Tully,⁶³ L. Uvarov,³⁶ S. Uvarov,³⁶

S. Uzunyan,⁴⁷ R. Van Kooten,⁴⁹ W.M. van Leeuwen,³⁰ N. Varelas,⁴⁶ E.W. Varnes,⁴² I.A. Vasilyev,³⁵ P. Verdier,¹⁷ A.Y. Verkheev,³² L.S. Vertogradov,³² M. Verzocchi,⁴⁵ M. Vesterinen,⁴¹ D. Vilanova,¹⁵ P. Vokac,⁷ H.D. Wahl,⁴⁴ M.H.L.S. Wang,⁴⁵ J. Warchol,⁵¹ G. Watts,⁷⁶ M. Wayne,⁵¹ J. Weichert,²¹ L. Welty-Rieger,⁴⁸ A. White,⁷² D. Wicke,²³ M.R.J. Williams,³⁹ G.W. Wilson,⁵³ M. Wobisch,⁵⁵ D.R. Wood,⁵⁷ T.R. Wyatt,⁴¹ Y. Xie,⁴⁵ R. Yamada,⁴⁵ S. Yang,⁴ W.-C. Yang,⁴¹ T. Yasuda,⁴⁵ Y.A. Yatsunenkov,³² W. Ye,⁶⁶ Z. Ye,⁴⁵ H. Yin,⁴⁵ K. Yip,⁶⁷ S.W. Youn,⁴⁵ J.M. Yu,⁵⁸ J. Zennamo,⁶⁴ T. Zhao,⁷⁶ T.G. Zhao,⁴¹ B. Zhou,⁵⁸ J. Zhu,⁵⁸ M. Zielinski,⁶⁵ D. Zieminska,⁴⁹ and L. Zivkovic⁷¹

(The D0 Collaboration*)

¹LAFEX, Centro Brasileiro de Pesquisas Físicas, Rio de Janeiro, Brazil

²Universidade do Estado do Rio de Janeiro, Rio de Janeiro, Brazil

³Universidade Federal do ABC, Santo André, Brazil

⁴University of Science and Technology of China, Hefei, People's Republic of China

⁵Universidad de los Andes, Bogotá, Colombia

⁶Charles University, Faculty of Mathematics and Physics,

Center for Particle Physics, Prague, Czech Republic

⁷Czech Technical University in Prague, Prague, Czech Republic

⁸Center for Particle Physics, Institute of Physics,

Academy of Sciences of the Czech Republic, Prague, Czech Republic

⁹Universidad San Francisco de Quito, Quito, Ecuador

¹⁰LPC, Université Blaise Pascal, CNRS/IN2P3, Clermont, France

¹¹LPSC, Université Joseph Fourier Grenoble 1, CNRS/IN2P3,

Institut National Polytechnique de Grenoble, Grenoble, France

¹²CPPM, Aix-Marseille Université, CNRS/IN2P3, Marseille, France

¹³LAL, Université Paris-Sud, CNRS/IN2P3, Orsay, France

¹⁴LPNHE, Universités Paris VI and VII, CNRS/IN2P3, Paris, France

¹⁵CEA, Irfu, SPP, Saclay, France

¹⁶IPHC, Université de Strasbourg, CNRS/IN2P3, Strasbourg, France

¹⁷IPNL, Université Lyon 1, CNRS/IN2P3, Villeurbanne, France and Université de Lyon, Lyon, France

¹⁸III. Physikalisches Institut A, RWTH Aachen University, Aachen, Germany

¹⁹Physikalisches Institut, Universität Freiburg, Freiburg, Germany

²⁰II. Physikalisches Institut, Georg-August-Universität Göttingen, Göttingen, Germany

²¹Institut für Physik, Universität Mainz, Mainz, Germany

²²Ludwig-Maximilians-Universität München, München, Germany

²³Fachbereich Physik, Bergische Universität Wuppertal, Wuppertal, Germany

²⁴Panjab University, Chandigarh, India

²⁵Delhi University, Delhi, India

²⁶Tata Institute of Fundamental Research, Mumbai, India

²⁷University College Dublin, Dublin, Ireland

²⁸Korea Detector Laboratory, Korea University, Seoul, Korea

²⁹CINVESTAV, Mexico City, Mexico

³⁰Nikhef, Science Park, Amsterdam, the Netherlands

³¹Radboud University Nijmegen, Nijmegen, the Netherlands

³²Joint Institute for Nuclear Research, Dubna, Russia

³³Institute for Theoretical and Experimental Physics, Moscow, Russia

³⁴Moscow State University, Moscow, Russia

³⁵Institute for High Energy Physics, Protvino, Russia

³⁶Petersburg Nuclear Physics Institute, St. Petersburg, Russia

³⁷Institució Catalana de Recerca i Estudis Avançats (ICREA) and Institut de Física d'Altes Energies (IFAE), Barcelona, Spain

³⁸Uppsala University, Uppsala, Sweden

³⁹Lancaster University, Lancaster LA1 4YB, United Kingdom

⁴⁰Imperial College London, London SW7 2AZ, United Kingdom

⁴¹The University of Manchester, Manchester M13 9PL, United Kingdom

⁴²University of Arizona, Tucson, Arizona 85721, USA

⁴³University of California Riverside, Riverside, California 92521, USA

⁴⁴Florida State University, Tallahassee, Florida 32306, USA

⁴⁵Fermi National Accelerator Laboratory, Batavia, Illinois 60510, USA

⁴⁶University of Illinois at Chicago, Chicago, Illinois 60607, USA

⁴⁷Northern Illinois University, DeKalb, Illinois 60115, USA

⁴⁸Northwestern University, Evanston, Illinois 60208, USA

⁴⁹Indiana University, Bloomington, Indiana 47405, USA

⁵⁰Purdue University Calumet, Hammond, Indiana 46323, USA

⁵¹University of Notre Dame, Notre Dame, Indiana 46556, USA

⁵²Iowa State University, Ames, Iowa 50011, USA

- ⁵³University of Kansas, Lawrence, Kansas 66045, USA
⁵⁴Kansas State University, Manhattan, Kansas 66506, USA
⁵⁵Louisiana Tech University, Ruston, Louisiana 71272, USA
⁵⁶Boston University, Boston, Massachusetts 02215, USA
⁵⁷Northeastern University, Boston, Massachusetts 02115, USA
⁵⁸University of Michigan, Ann Arbor, Michigan 48109, USA
⁵⁹Michigan State University, East Lansing, Michigan 48824, USA
⁶⁰University of Mississippi, University, Mississippi 38677, USA
⁶¹University of Nebraska, Lincoln, Nebraska 68588, USA
⁶²Rutgers University, Piscataway, New Jersey 08855, USA
⁶³Princeton University, Princeton, New Jersey 08544, USA
⁶⁴State University of New York, Buffalo, New York 14260, USA
⁶⁵University of Rochester, Rochester, New York 14627, USA
⁶⁶State University of New York, Stony Brook, New York 11794, USA
⁶⁷Brookhaven National Laboratory, Upton, New York 11973, USA
⁶⁸Langston University, Langston, Oklahoma 73050, USA
⁶⁹University of Oklahoma, Norman, Oklahoma 73019, USA
⁷⁰Oklahoma State University, Stillwater, Oklahoma 74078, USA
⁷¹Brown University, Providence, Rhode Island 02912, USA
⁷²University of Texas, Arlington, Texas 76019, USA
⁷³Southern Methodist University, Dallas, Texas 75275, USA
⁷⁴Rice University, Houston, Texas 77005, USA
⁷⁵University of Virginia, Charlottesville, Virginia 22901, USA
⁷⁶University of Washington, Seattle, Washington 98195, USA

(Dated: July 04, 2012)

We present a search for the standard model Higgs boson using events with two oppositely charged leptons and large missing transverse energy as expected in $H \rightarrow WW$ decays. The events are selected from data corresponding to 8.6 fb^{-1} of integrated luminosity in $p\bar{p}$ collisions at $\sqrt{s} = 1.96$ TeV collected with the D0 detector at the Fermilab Tevatron Collider. No significant excess above the standard model background expectation in the Higgs boson mass range this search is sensitive to is observed, and upper limits on the Higgs boson production cross section are derived.

PACS numbers: 14.80.Bn, 13.85.Qk, 13.85.Rm

INTRODUCTION

In the standard model (SM), the Higgs boson appears during the spontaneous breaking of the electroweak symmetry $SU(2) \times U(1)$ that is responsible for the generation of the masses of the W and Z bosons. Although the SM requires the existence of this neutral scalar particle, its mass (M_H) is a free parameter. Direct searches at the CERN e^+e^- collider (LEP) yield a lower limit of $M_H > 114.4 \text{ GeV}$ [1] at the 95% C.L. Precision electroweak data yield, including the latest W boson mass requirements from CDF [2] and D0 [3], constrain the mass of a SM Higgs boson to $M_H < 152 \text{ GeV}$ [4] at 95% C.L.

In this Article, we present a search for the SM Higgs boson in final states containing two oppositely charged leptons ($\ell\ell' = e\mu, ee, \text{ or } \mu\mu$, where small contributions

from leptonic τ decays are also included) and missing transverse energy (\cancel{E}_T), using 8.6 fb^{-1} of $p\bar{p}$ collisions collected with the D0 detector [5] at the Fermilab Tevatron Collider. These three leptonic final states are combined to produce a result which supersedes our previously published search for Higgs boson production in the oppositely charged dilepton and missing transverse energy final state based on data corresponding to an integrated luminosity of 5.4 fb^{-1} [6]. A similar search was published by the CDF Collaboration at the Tevatron using 4.8 fb^{-1} of integrated luminosity [7] and by the ATLAS and CMS Collaborations at the CERN Large Hadron Collider (LHC) using 4.7 fb^{-1} and 4.6 fb^{-1} of data, respectively [8, 9]. Using up to 5.4 fb^{-1} of integrated luminosity, the combination of the results from the Tevatron led to the first exclusion using the $H \rightarrow WW$ decays, excluding the Higgs boson beyond the LEP limits, in the mass range from 162 to 166 GeV at the 95% C.L. [12]. Recently, both ATLAS and CMS Collaborations have individually combined all their searches, and the results from ATLAS have excluded a Higgs boson in the mass range from 111.4 to 116.6, 119.4 to 122.1, 129.2 to 541 GeV, while results from CMS excluded a Higgs boson in the range 127 to 600 GeV at the 95% C.L. [10, 11].

The primary signal for opposite charge dilepton signa-

*with visitors from ^aAugustana College, Sioux Falls, SD, USA, ^bThe University of Liverpool, Liverpool, UK, ^cUPIITA-IPN, Mexico City, Mexico, ^dDESY, Hamburg, Germany, ^eSLAC, Menlo Park, CA, USA, ^fUniversity College London, London, UK, ^gCentro de Investigacion en Computacion - IPN, Mexico City, Mexico, ^hECFM, Universidad Autonoma de Sinaloa, Culiacán, Mexico and ⁱUniversidade Estadual Paulista, São Paulo, Brazil.

tures with considerable missing energy arises from production of Higgs bosons by gluon fusion $gg \rightarrow H$ with subsequent decay $H \rightarrow WW \rightarrow \ell\nu\ell'\nu'$. Additional contributions to this signature come from vector boson fusion (VBF), $qq' \rightarrow qq'H$, where the initial state partons radiate weak gauge bosons that then fuse to form a Higgs boson, and from production in association with a vector boson $qq' \rightarrow VH = (W/Z)H$. The dominant background contribution is from diboson production, in particular, contributions from non-resonant $p\bar{p} \rightarrow WW \rightarrow \ell\nu\ell'\nu'$ processes. Additionally, two types of instrumental backgrounds exist: 1) events with mismeasured \cancel{E}_T in the Drell-Yan process $p\bar{p} \rightarrow Z/\gamma^* \rightarrow \ell^+\ell^-$, which contribute particularly to the ee and $\mu\mu$ final states, and 2) events with jets misidentified as leptons and photons converting to electrons in W boson or multijet production. Although such false identification is rare, the resulting backgrounds are sizeable as the rates of W +jets and multijet production are significantly higher than that of Higgs boson production. Contributions in the $\mu\mu$ channel from falsely identified muons in W +jets events are relatively smaller.

The following Article first discusses the simulation methods used to predict the yields from signal and SM background processes. This is then followed by a brief description of the D0 detector and of the algorithms used to reconstruct and identify the objects used in the analysis. The event selection and the multivariate techniques used to separate the signal from the background are then discussed. The different sources of systematics uncertainties are then presented, followed by the results of the search for the Higgs boson.

EVENT SIMULATION

Higgs boson signal samples are simulated using the PYTHIA [13] Monte Carlo (MC) event generator with the CTEQ6L1 parton distribution functions (PDFs) [14] for $115 \leq M_H \leq 200$ GeV in increments of 5 GeV. The normalization of these MC samples is obtained using the highest-order cross section calculation available for the corresponding production process. The cross section for the gluon fusion process is calculated at next-to-next-to-leading order (NNLO) in quantum chromodynamics with soft gluon resummation to next-to-next-to-leading-log (NNLL) accuracy [15]. For WH , ZH and vector boson fusion processes, cross section calculations at NNLO are used [16, 17]. All signal cross sections are computed using the MSTW2008 PDF set [18]. The PDF uncertainties are assessed according to the recommendations given in Refs. [19, 20]. The Higgs boson branching ratio predictions are from HDECAY [21]. The distribution of the transverse momentum (p_T) of the Higgs boson in the PYTHIA-generated gluon fusion sample is reweighted to match the p_T as calculated by HQT, at NNLL and NNLO accuracy [22].

The dominant background processes for the search are Z/γ^* +jets, W +jets, diboson, $t\bar{t}$, and multijet production where jets can be misidentified as leptons. Electroweak single top quark production is not considered since its contribution is negligible. The W +jets and Z +jets backgrounds are modeled using ALPGEN [23], with showering and hadronization provided by PYTHIA. Diboson production processes (WW , WZ , and ZZ) are simulated using PYTHIA. The Z +jets and W +jets processes are normalized using the NNLO cross section calculations of Ref. [24] which uses the NLO CTEQ6.1 PDFs. The Z boson p_T distribution is weighted to match the distribution observed in data [25], taking into account its dependence on the number of reconstructed jets. The W boson p_T distribution is corrected to match the measured Z boson p_T spectrum [25] multiplied by the ratio of the W boson p_T to Z boson p_T distributions as predicted in NLO QCD [26]. For the search in the ee and $e\mu$ channels, the W +jets sample includes contributions from events in which a jet or a photon is misidentified as an electron. For $t\bar{t}$ production, approximate NNLO cross sections [27] are used, while the NLO production cross section values are used for WW , WZ , and ZZ processes [28]. For the irreducible background source, WW production, the p_T of the diboson system is modeled using the MC@NLO simulation [29]. All MC samples are processed through a GEANT simulation of the detector [30]. Recorded detector signals from randomly selected beam crossings with the same luminosity profile as data are added to the simulated detector signals of MC events in order to model effects of detector noise and additional $p\bar{p}$ interactions. The simulated background samples are subsequently normalized to the integrated luminosity.

DETECTOR AND OBJECT RECONSTRUCTION

The innermost part of the D0 detector [5] is composed of a central tracking system with a silicon microstrip tracker (SMT) and a central fiber tracker (CFT) embedded within a 2 T solenoidal magnet. The tracking system is surrounded by a central preshower detector (CPS) and a liquid-argon and uranium calorimeter with electromagnetic (EM), fine and coarse hadronic sections. A muon spectrometer resides beyond the calorimetry and is made of drift tubes, scintillation counters and toroidal magnets. The D0 detector was upgraded in Spring 2006 to include modifications to the trigger system [31] as well as an additional inner layer of silicon microstrip tracking installed near the beam pipe and referred to as Layer 0 [32]. The data used for this analysis include 1.1 fb^{-1} collected before these upgrades (Run IIa) and 7.5 fb^{-1} collected afterwards (Run IIb).

Electrons are identified as clusters in the EM calorimeter and are required to spatially match a track reconstructed in the central tracking detector. The electron

energy is measured from the calorimeter energy deposits within a cone of a radius $\mathcal{R} = \sqrt{(\Delta\eta)^2 + (\Delta\phi)^2} = 0.2$, in the four layers of the EM calorimeter and the first layer of the hadronic calorimeter, where η and ϕ are the pseudorapidity [33] and the azimuthal angle, respectively. Due to the different probabilities for jets and photons to be misidentified as electrons in the central (CC, $|\eta| < 1.1$) and the forward (EC, $|\eta| > 1.5$) calorimeter regions, different criteria are required for the electron clusters. The most important of these are: (1) calorimeter isolation f_{iso} less than 0.15 (CC) or less than 0.1 (EC), with $f_{\text{iso}} = [E_{\text{tot}}(\mathcal{R} < 0.4) - E_{\text{EM}}(\mathcal{R} < 0.2)]/E_{\text{EM}}(\mathcal{R} < 0.2)$, where E_{tot} is the total energy in the isolation cone of radius $\mathcal{R} = 0.4$ and E_{EM} is the EM energy in a cone of radius $\mathcal{R} = 0.2$; (2) an EM fraction f_{EM} larger than 0.9, where f_{EM} is the fraction of total energy deposited in the EM calorimeter, where the energies are measured within a cone of radius $\mathcal{R} = 0.2$; (3) a track isolation h_{iso} less than 3.5 GeV (CC) or less than $(-2.5 \times |\eta| + 7.0)$ GeV (EC), where h_{iso} is the scalar sum of the p_T of all tracks originating from the primary $p\bar{p}$ interaction vertex in an annulus $0.05 < \mathcal{R} < 0.4$ around the cluster; (4) a cluster shape consistent with that of an EM shower; (5) an eight-variable electron likelihood \mathcal{L}_8 that is required to be greater than 0.05, where \mathcal{L}_8 is constructed using the variables: f_{iso} , f_{EM} , h_{iso} , the ratio of the electron cluster energy to track momentum (E/p), the number of tracks within a cone of radius $\mathcal{R} = 0.4$, the track-cluster match probability computed from the spatial separation and the expected resolution, the track distance to the $p\bar{p}$ interaction vertex at closest approach (dca), and covariance matrices that contain variables that relate the energy deposits between various layers of the calorimeter as well as the longitudinal and lateral shower development; and (6) an artificial neural network trained using information from the tracker, calorimeter and CPS detector to further reject backgrounds from jets misidentified as electrons.

Muons are identified by the presence of at least one track segment, reconstructed in the muon spectrometer, that is spatially consistent with a track in the central detector. The momentum and charge are measured by the curvature of the central track. The muon candidate must pass quality requirements aimed at reducing false matching and background from cosmic rays. Muons are required to be isolated. The isolation variables are defined to be the scalar sum of the transverse energy in the calorimeter (ΣE_T^{calo}) within an annular cone $0.1 < \mathcal{R} < 0.4$ and the scalar sum of the transverse momenta (Σp_T^{trk}) of tracks within a cone $\mathcal{R} < 0.5$ around the muon candidate. In the $\mu\mu$ channel, the isolation variables for each muon must satisfy $\Sigma p_T^{\text{trk}} < 0.25 \times p_T^\mu$ and $\Sigma E_T^{\text{calo}} < 0.4 \times p_T^\mu$, p_T^μ being the momentum of the muon. Similarly in the $e\mu$ channel, the isolation variables must satisfy $\Sigma p_T^{\text{trk}} < 0.15 \times p_T^\mu$ and $\Sigma E_T^{\text{calo}} < 0.15 \times p_T^\mu$. For $e\mu$ and $\mu\mu$ channels, the momentum of the muon track, the momentum of the electron track, and the electron en-

ergy deposit in the calorimeter are not considered when calculating isolation variables for the other lepton. This prevents the presence of one lepton to spoil the isolation of the other lepton in events where the separation of leptons in (η, ϕ) space is smaller than $\mathcal{R} = 0.5$.

Jets are reconstructed from energy deposits in the calorimeter using Ban iterative midpoint cone algorithm with a cone radius of 0.5 [34]. All jets are required to have at least two associated tracks matched to the $p\bar{p}$ interaction vertex. The efficiency of this requirement is adjusted in the simulation to match that measured in data. Jets can be identified as likely containing b quarks (b -tagged) if they pass a selection cut on the output of a multivariate (MVA) based b -tagging discriminant, trained to separate b jets from light jets [35]. The jet energies are calibrated using transverse momentum balance in γ +jet events [36]. To account for differences in the quark/gluon jet composition between the γ +jet events and the W/Z +jet events, the jet energies are further corrected in simulated events to match those measured in Z +jets data. Comparison of ALPGEN with other generators [37] and with the data [38] shows discrepancies in jet η and dijet angular separation. Therefore a data based correction allows for a better modeling of these quantities in the ALPGEN Z/γ^* +jets samples.

The \cancel{E}_T is obtained from the vector sum of the transverse components of energy depositions in the electromagnetic and fine hadronic sections of the calorimeter and is corrected for any identified muons. All energy corrections to leptons and to jets are propagated to the \cancel{E}_T . Data based corrections are applied to MC samples which allow for a better modeling of the calorimeter response to unclustered objects.

In order to increase acceptance, all events satisfying any trigger requirement from the complete suite of triggers used for data taking are considered. While most of the candidate events in the analysis are selected by single-lepton and dilepton triggers, a gain in efficiency of up to 20%, depending on the channel is achieved by including events which pass lepton+jets and lepton+ \cancel{E}_T triggers.

EVENT SELECTION

Candidate events are selected by requiring at least two high- p_T oppositely charged leptons (e or μ), to originate from the same $p\bar{p}$ interaction vertex along the beam line (*i.e.*, within $\Delta z=2$ cm, where Δz is the distance between lepton tracks along the beam axis, measured at the distance of closest approach to this axis). Additional selections are carried out in two steps, “pre-selection” and the “final-selection”. The following section describes the selections imposed in each step and also outlines the additional kinematic and quality requirements for the search.

Preselection

In the $\mu\mu$ and ee channels, the two highest- p_T leptons are required to satisfy $p_T^{\ell_1} > 15$ GeV and $p_T^{\ell_2} > 10$ GeV respectively, whereas in the $e\mu$ channel, $p_T^e > 15$ GeV and $p_T^\mu > 10$ GeV are required. Electrons are required to be within the acceptances of the EM calorimeter and tracking system ($|\eta| < 1.1$ or $1.5 < |\eta| < 2.5$) and muons are restricted to the fiducial coverage of the muon system $|\eta| < 2.0$. In the ee channel, events are rejected when both electrons are found in the EC calorimeter as this eliminates only a small contribution to the signal which has poor signal to background ratio. Additionally, in the ee and $\mu\mu$ final states, the dilepton invariant mass $M_{\ell_1\ell_2}$ is required to be greater than 15 GeV. These criteria define the “preselection” stage of the analysis.

To correct for any possible mismodeling of the lepton reconstruction and trigger efficiencies, and to reduce the impact of the luminosity uncertainty, scale factors are applied to the MC samples at the preselection stage to match the data. The normalization factors are determined from Drell-Yan dominated samples within a dilepton mass window of $M_{\ell_1\ell_2} \in [80, 100]$ GeV for ee , $\mu\mu$ and $M_{\ell_1\ell_2} \in [57, 75]$ GeV for $e\mu$, and their differences from unity are smaller than the luminosity uncertainty. Figures 1–3 show a comparison between data and the background prediction for the distributions of the kinematic quantities for each of the dilepton final states after preselection requirements. In the dilepton mass distributions shown in Figs. 2a and 3a, the peak in the signal expectation at M_Z originates from ZH associated production where the two observed leptons are from the Z boson decay. The differences in the widths of the resonance in the ee and $\mu\mu$ channels is due to detector resolution. The transverse mass is defined as

$$M_T(\ell, \cancel{E}_T) = \sqrt{2 \cdot p_T^\ell \cdot \cancel{E}_T \cdot [1 - \cos \Delta\phi(\ell, \cancel{E}_T)]},$$

and consequently the minimal transverse mass, M_T^{\min} , shown in figs. 2d and 3d, is the minimum of the two $M_T(\ell, \cancel{E}_T)$ defined for each lepton.

Jets are considered in this analysis only if they have $p_T > 20$ GeV and $|\eta| < 2.4$. The preselected samples are further subdivided by the number of jets present in the event. Dividing the analysis into different jet multiplicity bins significantly increases the sensitivity of this search as the signal and background composition change between each sample. In particular, $gg \rightarrow H \rightarrow WW$ signal processes populate primarily the 0 and 1 jet multiplicity bins whereas contributions to higher multiplicity bins arise mainly from vector boson fusion production and associated VH processes which contain additional jets in the event. For the background, WW diboson production tends to dominate lower jet multiplicity bins while $t\bar{t}$ events generally contain two jets that are often b -tagged.

Subsequent analysis steps are carried out separately for events with zero jets, one jet, and two or more jets in order to optimally separate signal from backgrounds, resulting in a total of nine analysis channels (*i.e.*, three dilepton final states with three jet multiplicity bins each). The jet multiplicity spectrum of the simulated Z/γ^* sample is corrected to match that of the data for each channel considered. These corrections are derived within the mass windows as described above and have the primary effect of improving the ALPGEN modeling of $Z/\gamma^* + \text{jets}$.

The number of events for each jet multiplicity bin at preselection can be found in Table I. In general, good agreement between data and the expected background contribution is observed. At this stage, the Z/γ^* contribution is the dominant background source.

Final Selection

In the ee and $\mu\mu$ channels, a multivariate discriminant is used to remove the dominant Z/γ^* background present in the preselected data sample. The complete details are discussed later in this Article.

As the Z/γ^* contribution is smaller in the $e\mu$ channel, kinematic selections are instead applied to suppress backgrounds after preselection. For the signal, the \cancel{E}_T is not aligned with any of the leptons in the final state, while for the Z/γ^* background processes, the \cancel{E}_T is mostly caused by inaccurate measurements of the energies of the leptons and tends to point in the direction of one of the two leptons. Observables that take into account both the absolute value and the direction of the $\vec{\cancel{E}}_T$ are M_T^{\min} and M_{T2} , where M_{T2} is an extension of the transverse mass for final states with two visible and two invisible particles [39]. It is obtained as the minimum of the M_T^{\min} between either lepton and neutrino pair using a minimization procedure, where the sum of the momenta of the neutrinos is varied under the constraint that the sum of the momenta of the lepton pair is the missing transverse energy in the event. The distributions of these two observables in the $e\mu$ channel after the preselection are shown in Fig. 4 for each jet multiplicity bin. The requirements $M_T^{\min} > 20$ GeV and $M_{T2} > 15$ GeV define the final selection for this channel. The number of events at this selection stage for the $e\mu$ state can be found in Table II.

INSTRUMENTAL BACKGROUNDS

The main instrumental background processes for this analysis are due to (1) the mismeasurement of \cancel{E}_T in $Z/\gamma^* + \text{jets}$ events, (2) the misidentification of associated jets or photons in $W + \gamma/\text{jets}$ production as leptons, and (3) the misidentification of jets in multijet production as leptons.

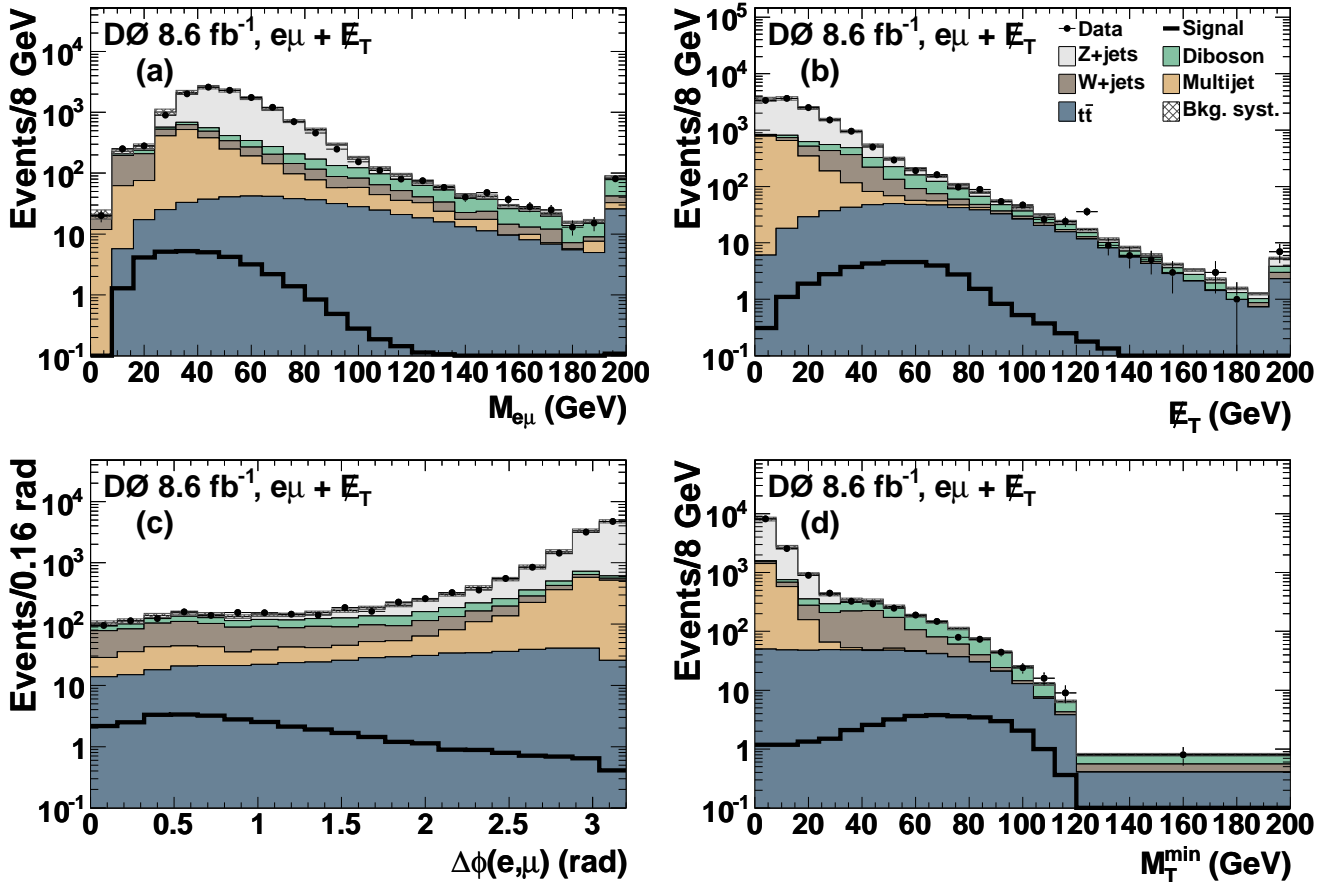


FIG. 1: [color online] The (a) dilepton invariant mass, (b) \cancel{E}_T , (c) $\Delta\phi$ between the leptons, and (d) minimum transverse mass for the $e\mu$ channel at the preselection stage. The last bin also includes all events above the upper range of the histogram (a,b,d). The signal distribution shown corresponds to a Higgs boson mass of 165 GeV. The hatched bands show the total systematic uncertainty on the background prediction.

TABLE I: Expected and observed numbers of events at preselection in the $e\mu$, ee , and $\mu\mu$ final states. The signal is for a Higgs boson mass of 165 GeV.

	Data	Total background	Signal	Z/γ^*	$t\bar{t}$	$W + \gamma/\text{jets}$	Dibosons	Multijet
$e\mu$:	13468	13754	35	9275	541	1066	842	2031
0 jets	10942	11171	20	8023	16	861	677	1594
1 jet	1849	1902	10	1088	157	154	142	362
≥ 2 jets	677	681	5	164	368	51	23	75
ee :	525942	524204	18	513365	244	1091	730	8776
0 jets	473311	472195	9	463751	9	840	425	7171
1 jet	42480	41795	5	40234	64	175	151	1172
≥ 2 jets	10151	10214	4	9380	171	76	154	433
$\mu\mu$:	724131	727456	26	723726	353	397	1107	1872
0 jets	624062	626473	13	624116	10	316	594	1437
1 jet	85349	85856	7	85069	90	68	280	348
≥ 2 jets	14720	15127	6	14541	253	13	233	87

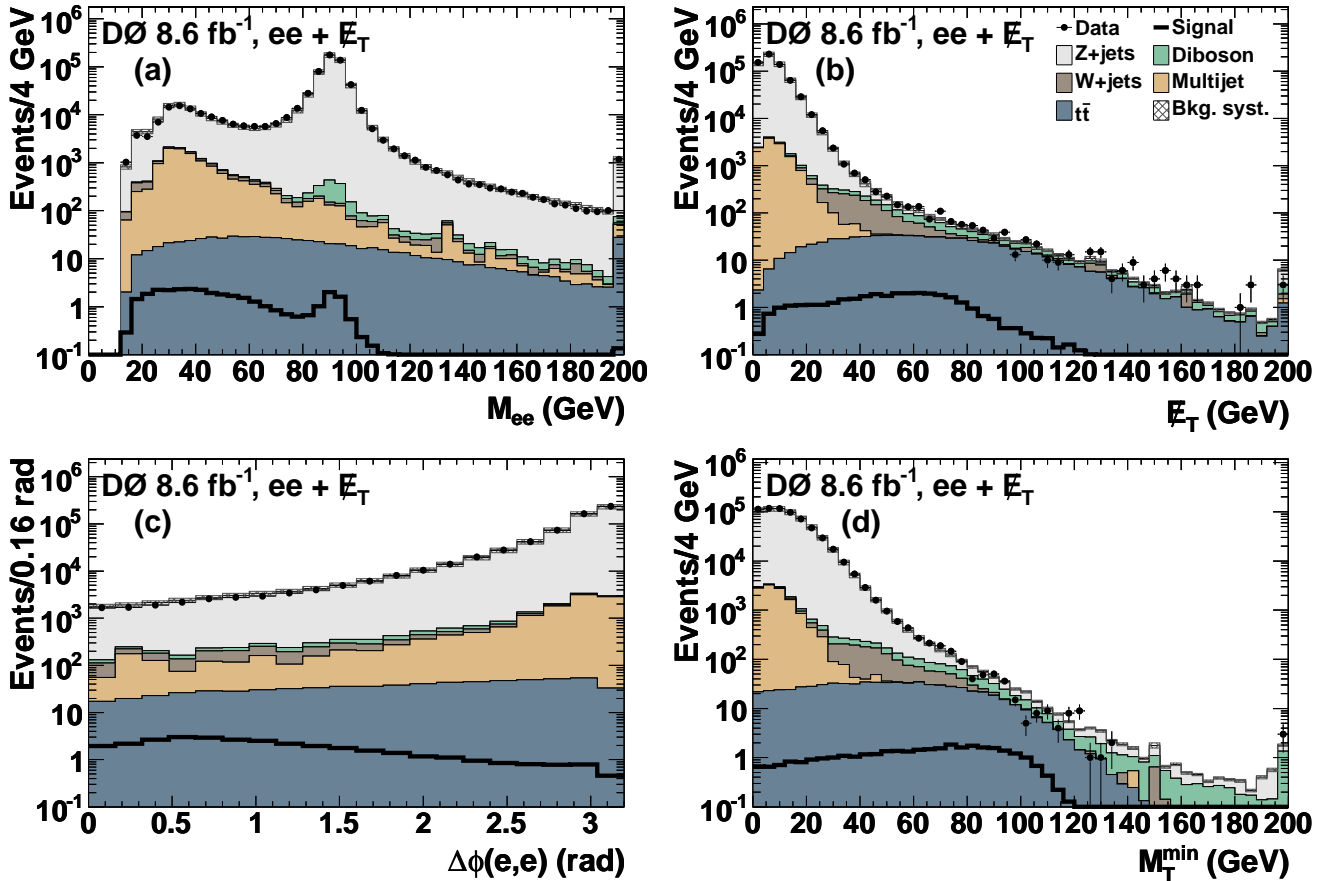


FIG. 2: [color online] The (a) dilepton mass, (b) \cancel{E}_T , (c) $\Delta\phi$ between the leptons, and (d) minimum transverse mass for the ee channel at the preselection stage. The last bin also includes all events above the upper range of the histogram (a,b,d). The signal distribution shown corresponds to a Higgs boson mass of 165 GeV. The hatched bands show the total systematic uncertainty on the background prediction.

Z and W Boson Production

Background contributions from Z bosons are estimated using MC simulations. The mismeasurement of \cancel{E}_T in $Z/\gamma^* + \text{jets}$ events adds a significant source of background particularly for the ee and $\mu\mu$ selections, as shown in Figs. 2b and 3b.

A W boson decaying leptonically and associated with one or more jets or a photon may contribute to the background if a jet is misidentified as a lepton or a photon overlaps an isolated track or converts into an electron-positron pair. The contribution from these backgrounds is estimated using MC simulations, and corrections to the contributions of jets and photons misidentified as electrons are derived using data, as explained below.

An enriched sample of $W + \gamma/\text{jets}$ not overlapping with the signal is selected from events passing all the selection criteria except that the charges of the two leptons are required to be identical. This requirement assumes that the probability of misidentifying a lepton as

a jet is independent of the lepton charge, and therefore, the like-charge dilepton sample can be used to estimate background corrections from misidentified leptons in the opposite-charge dilepton sample. Corrections are obtained separately for initial state radiation jets and photons ($\text{ISR}_{\gamma/j}$) and for final state radiation photons (FSR_{γ}) by splitting this control sample into high dilepton invariant mass ($M_{\ell_1\ell_2} > 40 \text{ GeV}$) and low dilepton invariant mass ($M_{\ell_1\ell_2} < 20 \text{ GeV}$) samples where the contributions of $\text{ISR}_{\gamma/j}$ and FSR_{γ} are, respectively, dominant. These corrections are applied in the ee and $e\mu$ final states, whereas they are not required in the $\mu\mu$ final state due to the smaller $W + \gamma/\text{jets}$ contribution.

Multijet Production

A high statistics sample of predominantly multijet events, where jets are misidentified as leptons, is obtained from data by inverting certain lepton selection

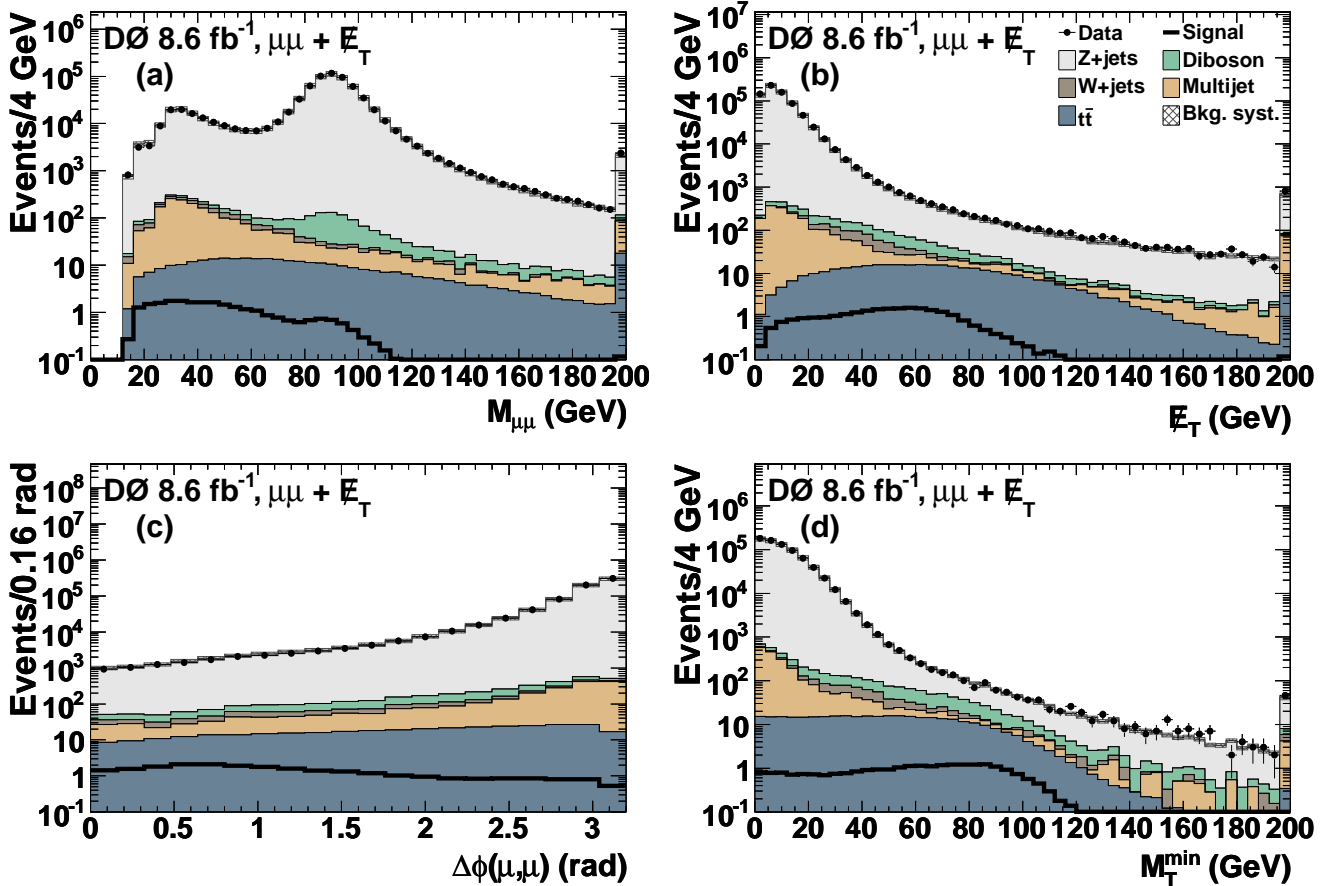


FIG. 3: [color online] The (a) dilepton mass, (b) \cancel{E}_T , (c) $\Delta\phi$ between the leptons, and (d) minimum transverse mass for the $\mu\mu$ channel at the preselection stage. The last bin also includes all events above the upper range of the histogram (a,b,d). The signal distribution shown corresponds to a Higgs boson mass of 165 GeV. The hatched bands show the total systematic uncertainty on the background prediction.

criteria. All other preselection criteria are applied in order to model the kinematic distributions of the multijet background in the signal region. In the $\mu\mu$ channel, the opposite-charge requirement for muons is reversed and a correction for the presence of non-multijet events in the like-charge sample, estimated from simulation, is applied. For the $e\mu$ and ee channels, the eight-variable electron likelihood selection is reversed, and to normalize the multijet sample to the actual contribution in the signal region, the multijet sample is compared to events which pass all the signal selections except that a like-charge requirement is imposed. This method accounts for any kinematic bias introduced from reversing the electron likelihood requirement. Since the probability of a jet being misidentified as a lepton (P_{lj}) is independent of charge, assuming that there is no correlation between the charges of the two misidentified leptons in multijet events, the like-charge sample has exactly the same normalization and kinematics as the actual multijet contribution. P_{lj} depends on the jet multiplicity, and therefore

the multijet background is estimated separately for each jet multiplicity bin. The analysis further assumes contributions of non-multijet processes are negligible in the reversed lepton quality sample.

MULTIVARIATE ANALYSIS

A multivariate technique is used to characterize events as originating from a Higgs boson signal or from background processes and to achieve maximum separation between them. A random forest of boosted decision trees (BDTs) [40] is used to construct a discriminant from kinematic variables, taking into account their correlations. The decision trees are trained separately in each of the nine analysis channels and for each Higgs boson mass hypothesis. To increase the statistics of the available simulated signal events, signal samples for neighboring mass hypotheses are used for the training of the multivariate discriminant. For example, the training of the

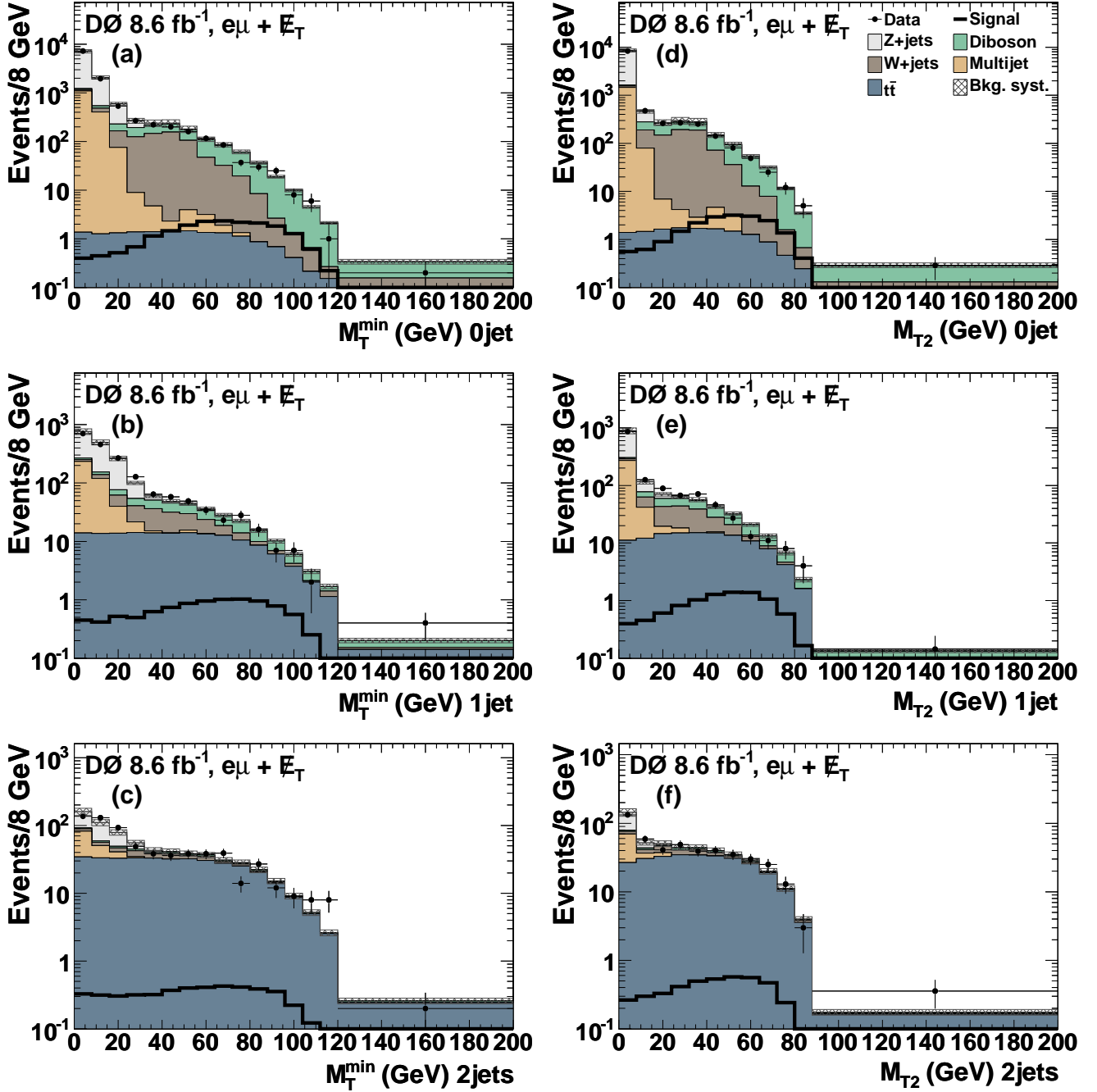


FIG. 4: [color online] M_T^{\min} distribution for the $e\mu$ channel in the (a) 0-jet bin, (b) 1-jet bin, and (c) ≥ 2 -jet bin. M_{T2} distribution for the $e\mu$ channel in the (d) 0-jet bin, (e) 1-jet bin, and (f) ≥ 2 -jet bin. The last bin also includes all events above the upper range of the histogram. The signal distribution shown corresponds to a Higgs boson mass of 165 GeV. The hatched bands show the total systematic uncertainty on the background prediction

discriminant for the 165 GeV mass hypothesis uses signal samples corresponding to a Higgs boson mass of 160, 165, and 170 GeV.

Multivariate Discriminant against Z/γ^*

A BDT discriminant is used in the ee and $\mu\mu$ final states to reject the large Z/γ^* background while retaining a high signal efficiency. This random forest of BDTs will be referred to as DY-BDT. The DY-BDT is trained

for each Higgs boson mass hypothesis and jet multiplicity bin, separately for the ee and $\mu\mu$ final states, to differentiate between the Z/γ^* background and all considered SM Higgs boson signal events.

The following input variables are used for the DY-BDT:

- (i) lepton p_T
- (ii) invariant mass of the leptons, $M_{\ell_1\ell_2}$
- (iii) azimuthal opening angle between the two leptons, $\Delta\phi(\ell_1, \ell_2)$
- (iv) separation in η, ϕ space between the two leptons, $\Delta R(\ell_1, \ell_2) = \sqrt{(\eta_{\ell_1} - \eta_{\ell_2})^2 + (\phi_{\ell_1} - \phi_{\ell_2})^2}$
- (v) minimal transverse mass, M_T^{\min}
- (vi) extended transverse mass, M_{T2}
- (vii) missing transverse energy, \cancel{E}_T
- (viii) smallest and largest of the azimuthal angles, $\Delta\phi$ between the \cancel{E}_T and either lepton
- (ix) transverse mass of the \cancel{E}_T and the dilepton pair, $M_T(\ell_1\ell_2, \cancel{E}_T)$
- (x) special missing transverse energy, $\cancel{E}_T^{\text{special}}$, defined for object ζ , which corresponds to either the nearest lepton or jet in the event relative to the direction of the \cancel{E}_T :

$$\cancel{E}_T^{\text{special}} = \begin{cases} \cancel{E}_T, & \text{if } \Delta\phi(\cancel{E}_T, \zeta) > \pi/2 \\ \cancel{E}_T \times \sin[\Delta\phi(\cancel{E}_T, \zeta)], & \text{otherwise} \end{cases}$$

- (xi) jet p_T
- (xii) scaled missing transverse energy defined as

$$\cancel{E}_T^{\text{scaled}} = \frac{\cancel{E}_T}{\sqrt{\sum_{\text{jets}} [\Delta E^{\text{jet}} \cdot \sin \theta^{\text{jet}} \cdot \cos \Delta\phi(\text{jet}, \cancel{E}_T)]^2}},$$

where ΔE^{jet} is a measure of jet energy resolution and is proportional to $\sqrt{E^{\text{jet}}}$; the fluctuation in the measurement of jet energy in the transverse plane can be approximated by the quantity $\Delta E^{\text{jet}} \cdot \sin \theta^{\text{jet}}$ [6]

- (xiii) azimuthal angle between the \cancel{E}_T and the jets, $\Delta\phi(\cancel{E}_T, \text{jet})$
- (xiv) absolute value of the pseudorapidity difference between the jets, $|\Delta\eta(j_1, j_2)|$, where j_1 and j_2 are the two highest- p_T jets in the event
- (xv) invariant mass of the two jets, $M(j_1, j_2)$.

Variables (i) and (ii) exploit the di-lepton kinematics of the event. Variables (iii) and (iv) are related to the opening angle between the two leptons and provide discrimination against SM backgrounds which tend to exhibit back-to-back topologies. This is not the case for Higgs boson decays because of the spin correlation in the scalar decay where leptons tend to be aligned in the same direction.

The \cancel{E}_T -related variables (v)–(ix) help distinguish genuine \cancel{E}_T in the Higgs boson signal from mismeasured \cancel{E}_T in Z/γ^* events. Variable (x) helps to further suppress Z/γ^* events, which populate lower values of $\cancel{E}_T^{\text{special}}$ where a mismeasured lepton or jet tends to align with the \cancel{E}_T direction [7]. Variables (xi)–(xv) are used in the 1-jet and 2-jet bins, as appropriate. Since the events are categorized in terms of jet multiplicities, variables (xii)–(xv) exploit the jet kinematics in the event.

To reject most of the Z/γ^* background after the pre-selection, events are required to appear in the signal-like region of the DY-BDT discriminant. This defines the final selection of the ee and $\mu\mu$ final states. The threshold varies for each Higgs boson mass hypothesis in each jet multiplicity bin and yields a Z/γ^* rejection factor of $\mathcal{O}(10^{-5})$, $\mathcal{O}(10^{-3})$, $\mathcal{O}(10^{-2})$ for the 0-jet, 1-jet, 2-jet bins, respectively for all dilepton channels and Higgs boson masses. The thresholds are chosen to obtain similar rejection factors of background events as the cut-based analysis employed in the previous publication [6]. The DY-BDT discriminants for a Higgs boson mass of 165 GeV are shown in Fig. 5. This figure demonstrates that a good separation is achieved between the Z/γ^* background and the majority of signal. However it can be noticed that some signal events cannot be distinguished from the background and have a very low DY-BDT discriminant value. This is primarily due to some of the Higgs decay modes which have a signature similar to Z/γ^* background. The numbers of events at the final selection stage for the ee and $\mu\mu$ final states are shown in Table II.

Final Multivariate Discriminant

In the final selection step, the signal is separated from the remaining backgrounds using an additional random forest of BDTs. This final random forest of BDTs referred to as FD-BDT, is trained for each Higgs boson mass hypothesis and jet multiplicity bin, separately for the three dilepton final states using signal and background samples, which satisfy the final selection criteria, to differentiate between all Higgs boson production processes and backgrounds. These decision trees use as inputs all the variables from the DY-BDT listed above with the addition of the following variables:

- (i) electron quality likelihood output, \mathcal{L}_S ; for the di-

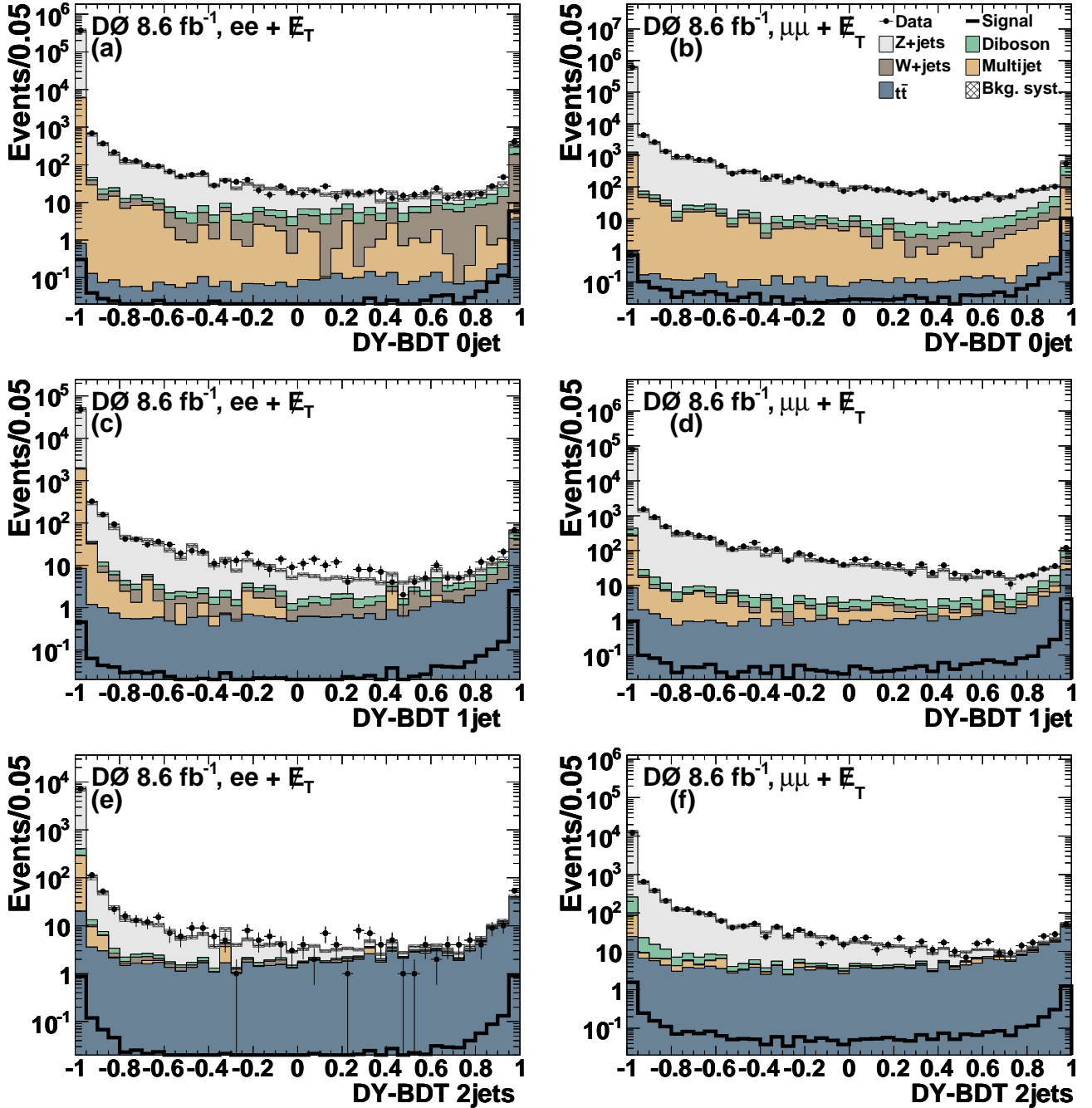


FIG. 5: DY-BDT discriminant for the 0-jet (top row), 1-jet (middle row) and ≥ 2 -jet (bottom row) for the ee [left (a,c,e)] and $\mu\mu$ [right (b,d,f)] final states. The discriminant shown is trained for a Higgs boson mass of 165 GeV. A final selection requirement is applied in the above distributions of 0.35, -0.6, and -0.85 for the ee final state and 0.9, 0., and -0.7 for the $\mu\mu$ final state, in the 0-jet, 1-jet, and ≥ 2 -jet bins, respectively. The hatched bands show the total systematic uncertainty on the background prediction.

electron channel the lower value of the two electron quality likelihood outputs is used

quality” and for the dimuon channel the lower quality of the two muons is used

(ii) a quality criterion based on the number of hits in the muon spectrometer characterized in four distinct categories; this parameter is referred to as “muon

(iii) number of Layer 0 hits in the SMT matched to each electron

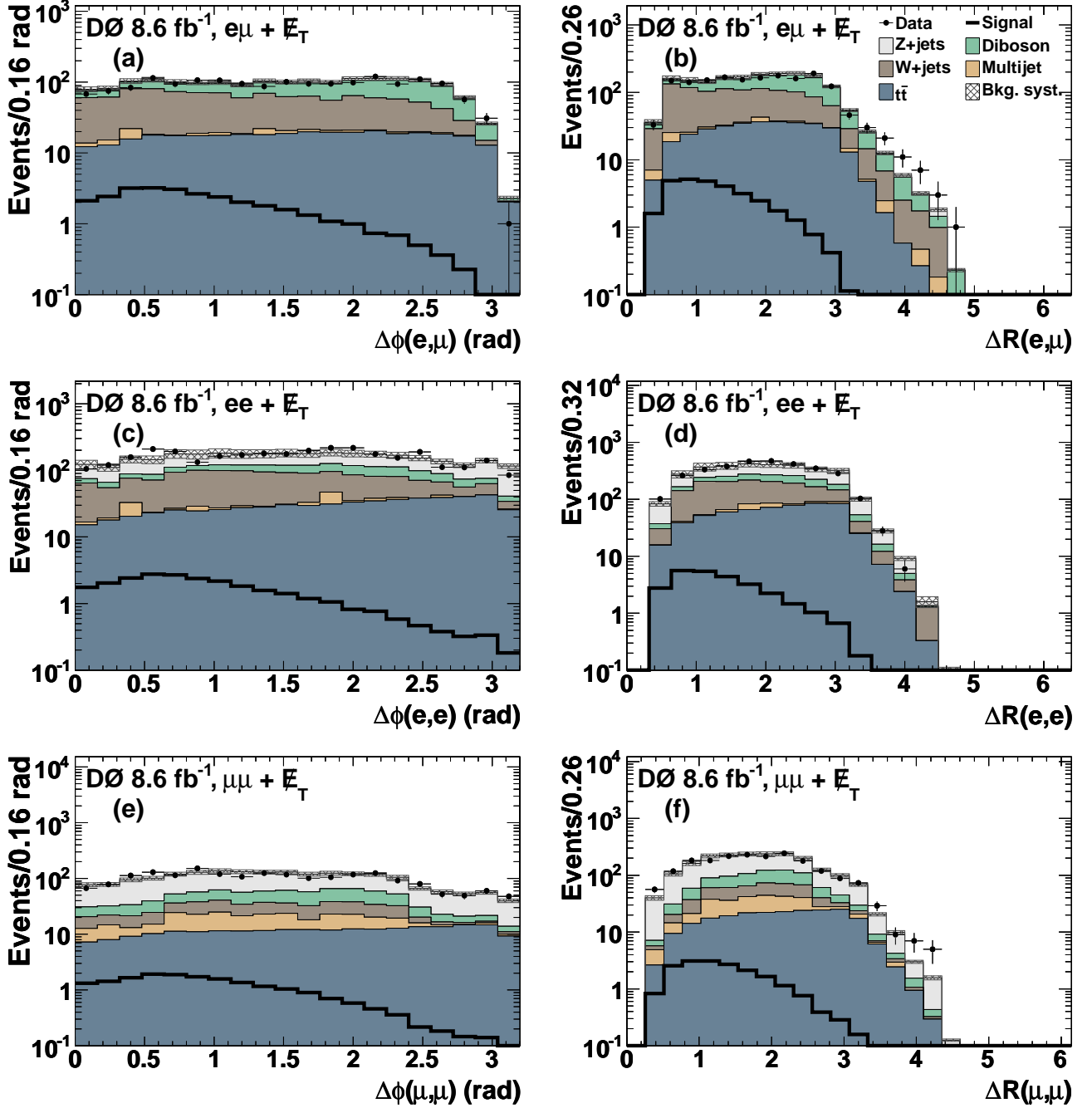


FIG. 6: [color online] The (left column) $\Delta\phi(\ell_1, \ell_2)$ and (right column) $\Delta R(\ell_1, \ell_2)$ for the $e\mu$ (a-b), ee (c-d) and $\mu\mu$ (e-f) channel at the final selection stage. The signal distribution shown corresponds to a Higgs boson mass of 165 GeV. The hatched bands show the total systematic uncertainty on the background prediction.

- (iv) track isolation variable of each muon
- (v) the product of charge and pseudorapidity, for both leptons ℓ_1 and ℓ_2
- (vi) b -tag output: the output of a multivariate discriminant to separate jets originating from heavy flavor quarks (b and c) from those originating from light

partons; for the channels with $N_{\text{jets}} \geq 2$, the smallest and largest b -tag outputs are used.

Some representative input distributions to the FD-BDT at the final selection stage with all jet multiplicity bins added in each distribution are shown in Figs. 6 and 7.

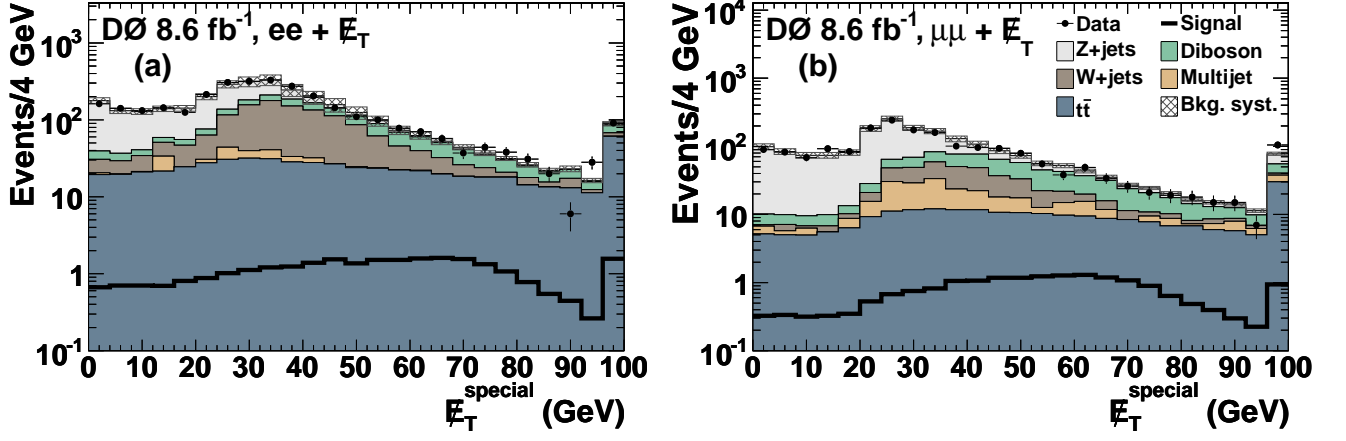


FIG. 7: [color online] The $\cancel{E}_T^{\text{special}}$ for the ee (a) and $\mu\mu$ (b) channel at the final selection stage. The last bin includes all events above the upper range of the histogram. The signal distribution shown corresponds to a Higgs boson mass of 165 GeV. The last bin also includes all events above the upper range of the histogram. The hatched bands show the total systematic uncertainty on the background prediction.

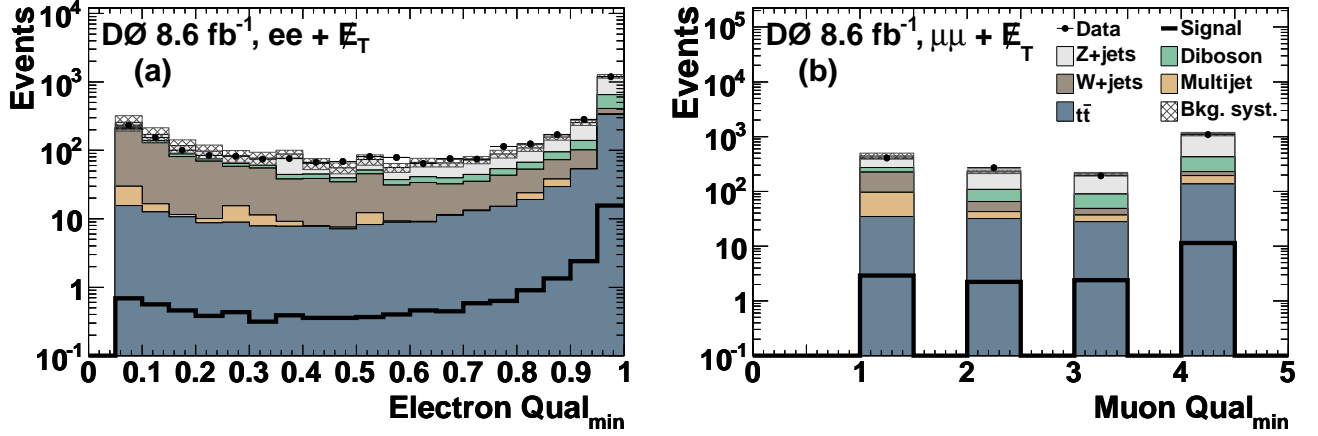


FIG. 8: [color online] The quality variable for (a) the ee channel and (b) the $\mu\mu$ channel at the final selection stage. The signal distribution shown corresponds to a Higgs boson mass of 165 GeV. The hatched bands show the total systematic uncertainty on the background prediction.

Representative distributions of the electron and muon quality variables, \mathcal{L}_8 and “muon quality,” are shown in Fig. 8. These along with other variables given in (iii) and (iv) gauge the quality of the reconstruction of the lepton and are crucial to discriminate between true leptons and jets misidentified as leptons originating from backgrounds like W +jets. The distribution for the product of charge and pseudorapidity, is symmetric in η for the signal, however this is not true for the background processes with misidentified leptons.

The output from b -tagging is used to separate the Higgs boson signal from $t\bar{t}$ production, which is an important background in the 1 and 2 jet multiplicity bins. An MVA-based b -tagging [35] is employed in each of the dilepton final states to discriminate the signal, which

comprises primarily light flavor quarks, against the heavy flavor jets arising from top quark decays. The distributions for smallest and largest b -tagging output in the ≥ 2 -jet multiplicity bin are shown in Fig. 9.

The distributions of the final BDT discriminant for each channel and Higgs boson masses of 125 GeV and 165 GeV are shown in Figs. 10 – 12.

SYSTEMATIC UNCERTAINTIES

Systematic uncertainties are characterized for each final state, background, and signal processes. Uncertainties that modify only the normalization and uncertainties that change the shape of the final discriminant distri-

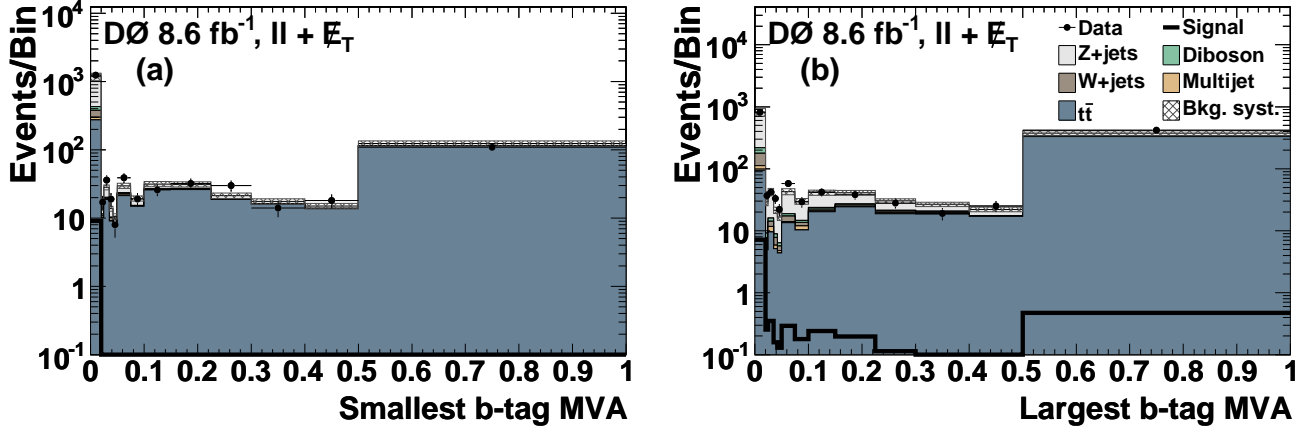


FIG. 9: [color online] The (a) smallest b -tagging MVA output and (b) largest b -tagging MVA output for the ≥ 2 -jet multiplicity bin, for all channels summed up at the final selection stage. The signal distribution shown corresponds to a Higgs boson mass of 165 GeV. The hatched bands show the total systematic uncertainty on the background prediction.

TABLE II: Expected and observed numbers of events after the final selection in the $e\mu$, ee , and $\mu\mu$ final states. The signal is for a Higgs boson mass of 165 GeV.

	Data	Total background	Signal	Z/γ^*	$t\bar{t}$	$W + \gamma/\text{jets}$	Dibosons	Multijet
$e^\pm\mu^\mp$:	1729	1806	30	94	335	766	584	29
0 jets	1117	1222	18	70	11	641	486	15
1 jet	335	307	8	19	98	94	87	10
≥ 2 jets	277	277	4	5	226	31	11	4
ee :	1607	1644	14	466	200	658	288	33
0 jets	812	881	8	135	6	499	222	20
1 jet	430	408	4	181	54	114	52	7
≥ 2 jets	365	355	2	150	140	45	14	6
$\mu\mu$:	1950	1997	18	1101	231	198	328	140
0 jets	645	720	10	227	4	155	236	98
1 jet	581	564	5	376	56	35	68	30
≥ 2 jets	724	713	3	498	171	8	24	12

tribution are taken into account. Systematic uncertainties that contribute only to the normalization are: theoretical cross sections for diboson, 6%, and $t\bar{t}$ production, 7%; multijet normalization, 30%; overall normalization, 4%, which accounts for the uncertainty on the lepton trigger/identification efficiency and the integrated luminosity; and a Z +jets jet-bin-dependent normalization (2–15)%.

Since the analysis is split into categories depending on the number of reconstructed jets, renormalization and factorization scale uncertainties on $\sigma(gg \rightarrow H)$ are estimated following the prescription described in Ref. [41]. By propagating the uncorrelated uncertainties of the NNLL inclusive [15, 42], NLO ≥ 1 jet [20], and NLO ≥ 2 jets [43] cross sections to the exclusive $gg \rightarrow H+0$ jet, ≥ 1 jet, and ≥ 2 jets rates, the uncertainty matrix shown in Table III is built. The PDF uncertainties for $\sigma(gg \rightarrow H)$, obtained using the prescription in Refs. [15, 20], are also summarized in Table III. The uncertainties on the inclu-

sive $\sigma(VH)$ and $\sigma(qqH)$ are taken as 6% and 5%, respectively.

Sources of systematic uncertainty that affect both the normalization and the shape of the final discriminant distribution are: jet energy scale (1–4)% and jet energy resolution (1–3)%, determined by varying the parameters of the energy scale correction and the energy resolution function within one standard deviation (s.d.) of the uncertainty and repeating the analysis using the kinematics of the modified jets; jet association to the $p\bar{p}$ interaction vertex (1–2)%, obtained by varying the correction factor within its uncertainty; shape of the b -tagging discriminant associated with heavy flavor jets (3–5)%, determined by varying the correction factor of the b -tagging neural network output within its uncertainty; W +jets modeling (6–50)%, depending on jet multiplicity bin and final state, obtained by varying the correction factors described in the “Instrumental Backgrounds” sec-

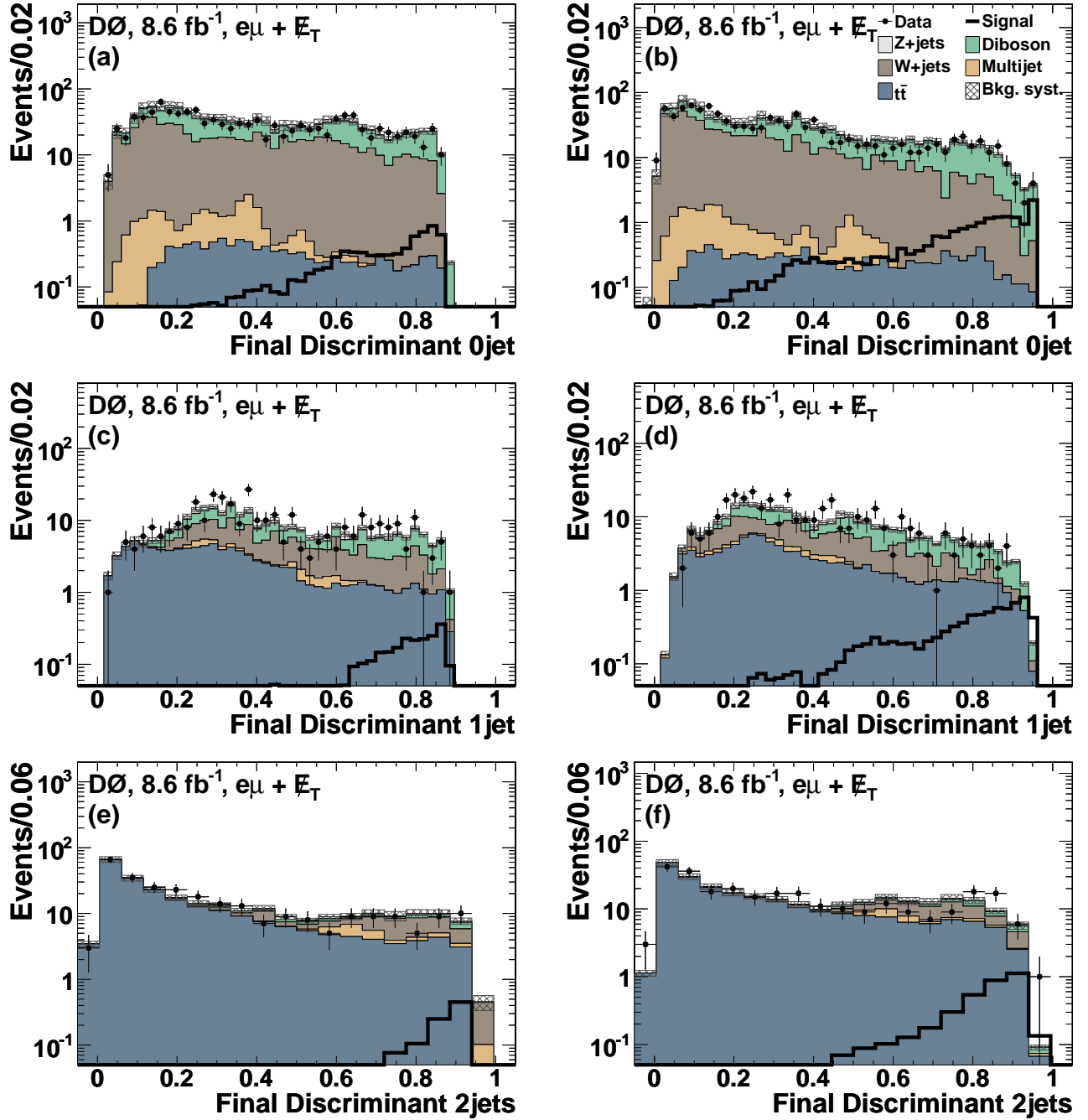


FIG. 10: [color online] Final BDT discriminant for the (top-row) 0-jet, (middle-row) 1-jet, and (bottom-row) ≥ 2 -jet bins for the $e\mu$ final state for a Higgs boson masses of 125 GeV [left (a,c,e)] and 165 GeV [right (b,d,f)]. The hatched bands show the total systematic uncertainty on the background prediction.

tion within their uncertainties. These uncertainties are presented in terms of the average fractional change across bins of the final discriminant distribution for all backgrounds and depend on the jet multiplicity.

Several systematic uncertainties are also included which have a small ($< 1\%$) effect on the background model: modeling of diboson production in terms of

$p_T(WW)$, determined by taking the fractional difference of the predicted final discriminant shape between MC@NLO and PYTHIA generators; modeling of diboson production in terms of the impact of the gluon fusion production process on the $\Delta\phi$ distribution between the leptons, determined by taking the fractional difference of the predicted final discriminant shape between MC@NLO

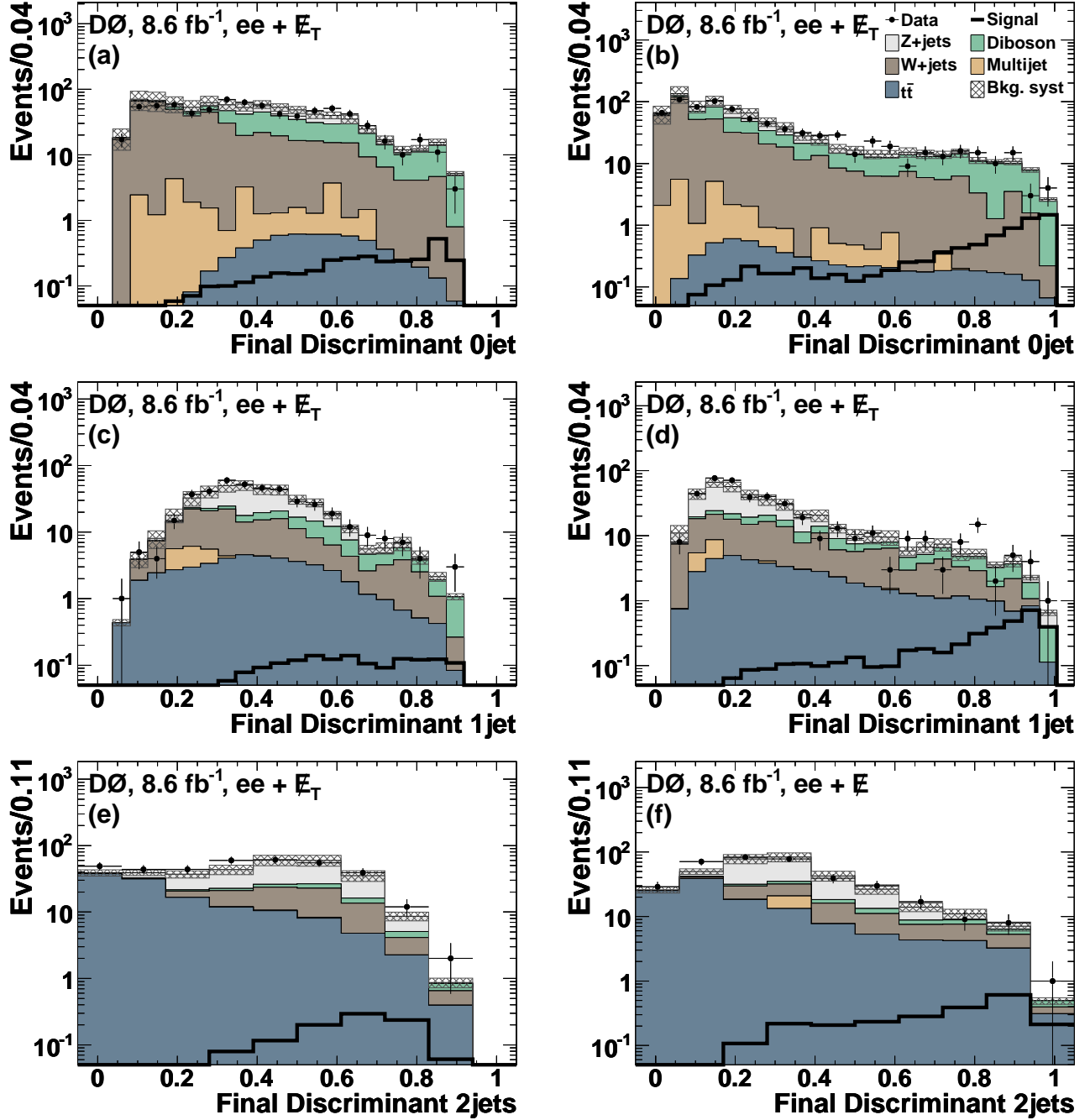


FIG. 11: [color online] Final BDT discriminant for the (top-row) 0-jet, (middle-row) 1-jet, and (bottom-row) ≥ 2 -jet bins for the ee final state for a Higgs boson masses of 125 GeV [left (a,c,e)] and 165 GeV [right (b,d,f)]. The hatched bands show the total systematic uncertainty on the background prediction.

and GG2WW [44] generators; and the p_T of the vector boson from W +jets and Z +jets production. A summary of the dominant systematic uncertainties is given in Table IV.

RESULTS

The methodology of this search is validated by an independent measurement of the $p\bar{p} \rightarrow W^+W^-$ cross section using the analysis procedure described in the “Event Selection” section of this Article, considering WW events as the signal. This is motivated by the fact that WW

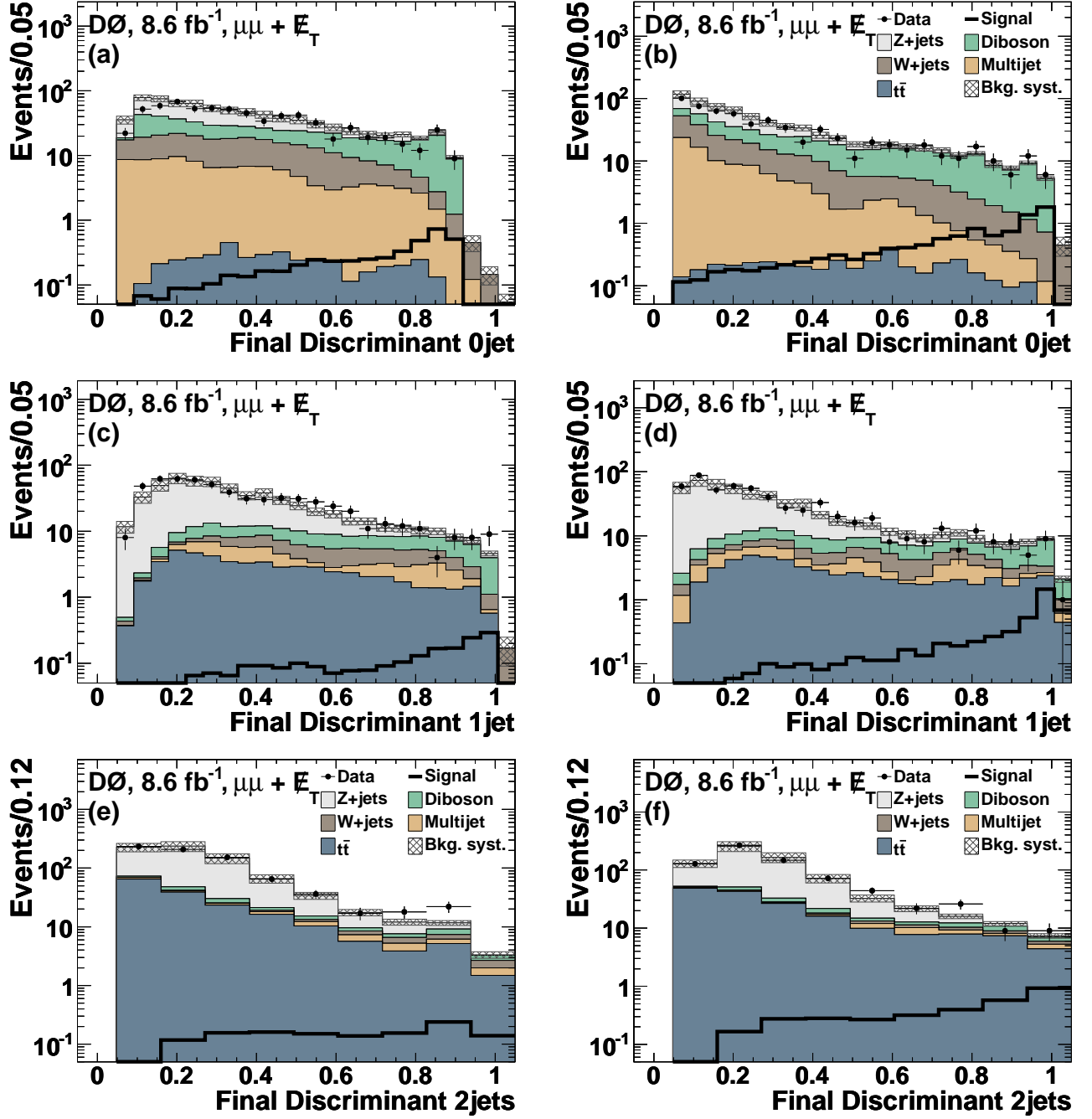


FIG. 12: [color online] Final BDT discriminant for the (top-row) 0-jet, (middle-row) 1-jet, and (bottom-row) ≥ 2 -jet bins for the $\mu\mu$ final state for a Higgs boson masses of 125 GeV [left (a,c,e)] and 165 GeV [right (b,d,f)]. The hatched bands show the total systematic uncertainty on the background prediction.

TABLE III: Elements of the uncertainty matrix of the scale (μ_R, μ_F) and PDF uncertainties on $\sigma(gg \rightarrow H)$ for the three jet multiplicity categories considered, where s_0, s_1 and s_2 are the elements of the uncertainty matrix.

σ μ_R, μ_F	s_0	s_1	s_2	PDF
0 jet	13.4 %	-23.0 %	-	7.6 %
≥ 1 jet	-	35.0 %	-12.7 %	13.8, %
≥ 2 jets	-	-	33.0 %	29.7 %

TABLE IV: Summary of systematic uncertainties (in %) for source categories. The jet, b -tagging and PDF related uncertainties are quoted for all the backgrounds combined.

Source	Uncertainty (%)
Overall normalization	4.0
W +jets normalization	6.0–50.0
Diboson cross section	6.0
$t\bar{t}$ cross section	7.0
Multijet normalization	30.0
Z +jets jet-bin normalization	2.0–15.0
$gg \rightarrow H$ cross section	See Table III
VH cross section	6.0
qqH cross section	5.0
Jet energy scale	1.0–4.0
Jet resolution	1.0–3.0
Jet primary vertex association	1.0–2.0
b -tagging discriminant	1.0–2.0
PDF (background)	2.5

production is the main contributor to the diboson entry in both Tables I and II compared to the expected yields from WZ and ZZ production backgrounds. Similarly to the Higgs boson search, a dedicated BDT is constructed, but now it is trained to separate WW production signal from other SM processes. For this BDT, we use the identical input variables, the same separation method in terms of jet multiplicity bins, and the same treatment of systematic uncertainties as in the Higgs boson search. The ee and $\mu\mu$ final states use only the 0 and 1 jet multiplicity bins while the $e\mu$ final state uses all three jet multiplicity bins yielding a total of seven analysis channels for the combination. The results obtained for the WW cross section in the individual final states and their combination are summarized in Table V. The measured value of 11.1 ± 0.8 pb is in good agreement with the SM prediction of 11.7 ± 0.8 pb [28]. The presence of a Higgs boson signal in the mass range $115 < M_H < 180$ GeV would bias the cross section measurement result by 5% at most. This maximum bias is reached for $M_H = 165$ GeV, but at low masses ($M_H < 130$ GeV), the bias would be less than 2%.

Figures 13 and 14 show the expected WW and Higgs boson signals, respectively, for the combined decay channels in the analysis. In these distributions, the data is shown, ordered in bins of increasing values of the s/b ratio, after the subtraction of the SM backgrounds. The background model is fit to the data, and the uncertainties on the background are those after the systematic uncertainties have been constrained by the fit.

The final multivariate discriminants of the SM Higgs boson search, shown in Figs. 10 – 12, demonstrate that the data is well described by the sum of the background predictions. In the absence of an excess in the number of observed events above the SM backgrounds, these

BDT output distributions are used to set upper limits on the Higgs boson inclusive production cross section $\sigma(p\bar{p} \rightarrow H + X)$ assuming SM values for the branching ratios and for the relative cross sections of the various Higgs production mechanisms considered. The limits are calculated using a modified frequentist method with a log-likelihood ratio (LLR) test statistic [45]. The value of CL_s is defined as $CL_s = CL_{s+b}/CL_b$, where CL_{s+b} and CL_b are the p -values for the signal+background and background-only hypotheses, respectively. Expected limits are calculated from the background-only LLR distribution whereas the observed limits are quoted with respect to the LLR values measured in data. They both are reported at the 95% C.L.

The multivariate discriminants corresponding to the nine individual channels are all used to obtain upper limits on the Higgs boson production cross section. Given the differences in the background contributions to each of the channels, the nine BDT output distributions are not combined in a single distribution for the limit extraction, but treated separately. The degrading effects of systematic uncertainties on the search sensitivity are minimized by fitting individual background contributions to the data by maximizing a profile likelihood function for the background-only and signal+background hypotheses separately, taking into account appropriately all correlations between the systematic uncertainties [46]. Table VI and Fig. 15 present expected and observed upper limits at the 95% C.L. for $\sigma(p\bar{p} \rightarrow H + X)$ relative to SM predictions for each Higgs boson mass considered.

The corresponding LLR distributions are shown in Fig. 16. Included in this plot are the median of the LLR distributions for the background-only hypothesis (LLR_b), the signal-plus-background hypothesis (LLR_{s+b}), and the observed value for the data (LLR_{obs}). The shaded

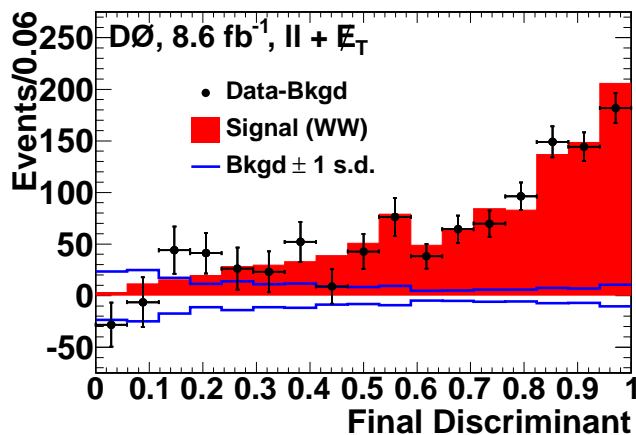


FIG. 13: [color online] The background-subtracted data distribution for the final discriminant, summed in bins with similar signal to background ratio, for the WW cross section measurement. The uncertainties shown on the background-subtracted data points are the square roots of the post-fit background predictions in each bin, representing the expected statistical uncertainty on the data. Also shown is the ± 1 standard deviation (s.d.) band on the total background after fitting.

TABLE V: Summary of the measurements of the $p\bar{p} \rightarrow W^+W^-$ cross section measurement (in pb) in all seven channels considered and their combination.

Channel	$\sigma(p\bar{p} \rightarrow W^+W^-)$
$e\mu$	10.6 ± 0.6 (stat) ± 0.6 (syst)
ee	12.4 ± 1.2 (stat) ± 0.9 (syst)
$\mu\mu$	11.0 ± 0.9 (stat) ± 0.7 (syst)
Combined	11.1 ± 0.5 (stat) ± 0.6 (syst)

bands represent one and two s.d. departures for LLR_b centered on the median. The separation between the LLR_b and LLR_{s+b} distributions provides a measure of the discriminating power of the search. The current result indicates that the signal+background model can be separated from the background-only model by up to 1 s.d. over most Higgs boson masses between 115 to 200 GeV while the level of separation increases above 2 s.d. for Higgs boson masses between 160 to 170 GeV. The sensitivity of the search reaches an expected exclusion of $159 < M_H < 169$ GeV at 95% C.L. However due to a slight excess in the data, an observed exclusion is not obtained.

CONCLUSIONS

We have performed a search for SM Higgs boson production using final states with two oppositely charged leptons and large missing transverse energy in the $e\mu$, ee , and $\mu\mu$ channels. After imposing all selection criteria, no significant excess in data over expected SM backgrounds is observed. We set upper limits on Higgs boson production at the 95% C.L. The sensitivity of the search reaches an expected exclusion of $159 < M_H < 169$ GeV.

The best observed limit is obtained at 160 GeV, where it reaches 1.1 times the SM expectation. This channel is the single most sensitive channel when the $H \rightarrow WW$ branching ratio is dominant ($M_H > 135$ GeV), and for lower masses at $M_H = 125$ GeV, this search still has a similar sensitivity as a single major low mass channel (WH or ZH) with an expected limit of 3.8 times the SM expectation [47]. The results and the analysis techniques are validated through an independent measurement of the WW production cross section, which agrees with the NNLO calculation.

ACKNOWLEDGMENTS

We thank the staffs at Fermilab and collaborating institutions, and acknowledge support from the DOE and NSF (USA); CEA and CNRS/IN2P3 (France); MON, Rosatom and RFBR (Russia); CNPq, FAPERJ, FAPESP and FUNDUNESP (Brazil); DAE and DST (India); Colciencias (Colombia); CONACyT (Mexico); NRF (Korea); FOM (The Netherlands); STFC and the Royal Society (United Kingdom); MSMT and GACR (Czech Republic); BMBF and DFG (Germany); SFI (Ireland); The Swedish Research Council (Sweden); and CAS and

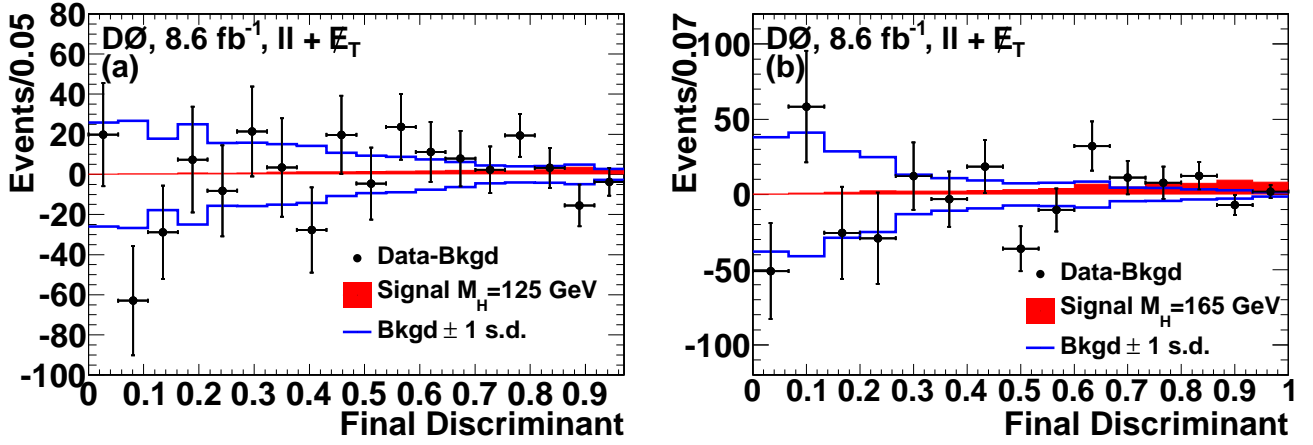


FIG. 14: [color online] The background-subtracted data distributions for the final discriminants, summed in bins with similar signal to background ratio, for (a) $M_H = 125$ GeV and (b) $M_H = 165$ GeV. The uncertainties shown on the background-subtracted data points are the square roots of the post-fit background predictions in each bin, representing the expected statistical uncertainty on the data. Also shown is the ± 1 standard deviation (s.d.) band on the total background after fitting.

TABLE VI: Expected and observed upper limits at the 95% C.L. for $\sigma(p\bar{p} \rightarrow H + X)$ relative to the SM for the total combination and separately for the $e\mu$, ee and $\mu\mu$ channels for different Higgs boson masses (M_H).

M_H (GeV)	115	120	125	130	135	140	145	150	155	160	165	170	175	180	185	190	195	200
Exp. all:	8.00	5.37	3.81	3.02	2.43	2.09	1.77	1.53	1.28	0.92	0.85	1.05	1.27	1.49	1.88	2.48	2.87	3.32
Obs. all:	13.27	9.14	5.00	4.71	3.93	3.28	2.13	1.99	1.75	1.10	1.17	1.40	1.40	1.64	1.91	2.34	2.87	3.50
Exp. $e\mu$	11.25	7.08	5.07	4.01	3.18	2.76	2.29	1.93	1.60	1.21	1.13	1.39	1.64	1.96	2.48	3.12	3.66	4.24
Obs. $e\mu$	13.86	8.50	5.12	4.62	4.01	2.61	1.96	1.68	1.47	1.10	1.27	1.38	1.60	1.68	2.28	2.52	2.84	3.39
Exp. ee	16.07	11.53	8.08	6.30	4.84	4.05	3.60	3.12	2.65	1.92	1.82	2.11	2.63	3.07	3.66	4.76	5.84	6.52
Obs. ee	19.37	13.93	10.08	9.12	6.31	6.65	4.78	4.95	4.52	2.61	2.88	3.35	3.16	4.82	4.55	7.12	8.26	9.24
Exp. $\mu\mu$	15.09	9.97	7.08	5.44	4.56	3.92	3.37	2.93	2.60	1.99	1.83	2.29	2.72	3.24	4.16	5.08	5.68	6.89
Obs. $\mu\mu$	25.84	18.83	9.93	8.34	7.01	7.11	5.37	4.45	3.88	2.99	2.31	3.22	3.79	4.19	5.16	5.78	7.98	8.42

CNSF (China).

- [1] R. Barate *et al.*, Phys. Lett. B **565**, 61 (2003).
- [2] T. Aaltonen *et al.* [CDF Collaboration], Phys. Rev. Lett. **108**, 151803 (2012).
- [3] V. M. Abazov *et al.* [D0 Collaboration], Phys. Rev. Lett. **108**, 151804 (2012).
- [4] The LEP Electroweak Working group, “Status of March 2012”, <http://lepewwg.web.cern.ch/LEPEWWG>.
- [5] V. M. Abazov *et al.* [D0 Collaboration], Nucl. Instrum. Meth. in Phys. Res. A **565**, 463 (2006).
- [6] V. M. Abazov *et al.* [D0 Collaboration], Phys. Rev. Lett. **104**, 061804 (2010).
- [7] T. Aaltonen *et al.* [CDF Collaboration], Phys. Rev. Lett. **104**, 061803 (2010).
- [8] G. Aad *et al.* [ATLAS Collaboration], submitted to Phys. Lett. B, arXiv:1206.0756 [hep-ex] (2012).
- [9] S. Chatrchyan *et al.* [CMS Collaboration], Phys. Lett. B **710**, 91 (2012).
- [10] G. Aad *et al.* [ATLAS Collaboration], submitted to Phys. Rev. D, arXiv:1207.0319 [hep-ex] (2012).
- [11] S. Chatrchyan *et al.* [CMS Collaboration], Phys. Lett. B **710**, 26 (2012).
- [12] T. Aaltonen *et al.* [CDF and D0 Collaborations], Phys. Rev. Lett. **104**, 061802 (2010).
- [13] T. Sjöstrand, S. Mrenna, and P. Skands, J. High Energy Phys. **05**, 026 (2006).
- [14] J. Pumplin *et al.*, J. High Energy Phys. **07**, 12 (2002).
- [15] D. de Florian and M. Grazzini, Phys. Lett. B **674**, 291 (2009).
- [16] J. Baglio and A. Djouadi, J. High Energy Phys. **10**, 064 (2010).
- [17] P. Bolzoni *et al.*, Phys. Rev. Lett. **105**, 011801 (2011).
- [18] A. D. Martin, W. J. Stirling, R. S. Thorne, and G. Watt, Eur. Phys. J. C **63**, 189 (2009).
- [19] S. Alekhin *et al.* [PDF4LHC Working Group], arXiv:1101.0536 [hep-ph]; M. Botje *et al.* [PDF4LHC Working Group], arXiv:1101.0538 [hep-ph].
- [20] C. Anastasiou, G. Dissertori, M. Grazzini, F. Stöckli, and B. R. Webber, J. High Energy Phys. **08**, 099 (2009).
- [21] A. Djouadi, J. Kalinowski, and M. Spira, Comput. Phys. Commun. **108**, 56 (1998).
- [22] G. Bozzi, S. Catani, D. de Florian, and M. Grazzini,

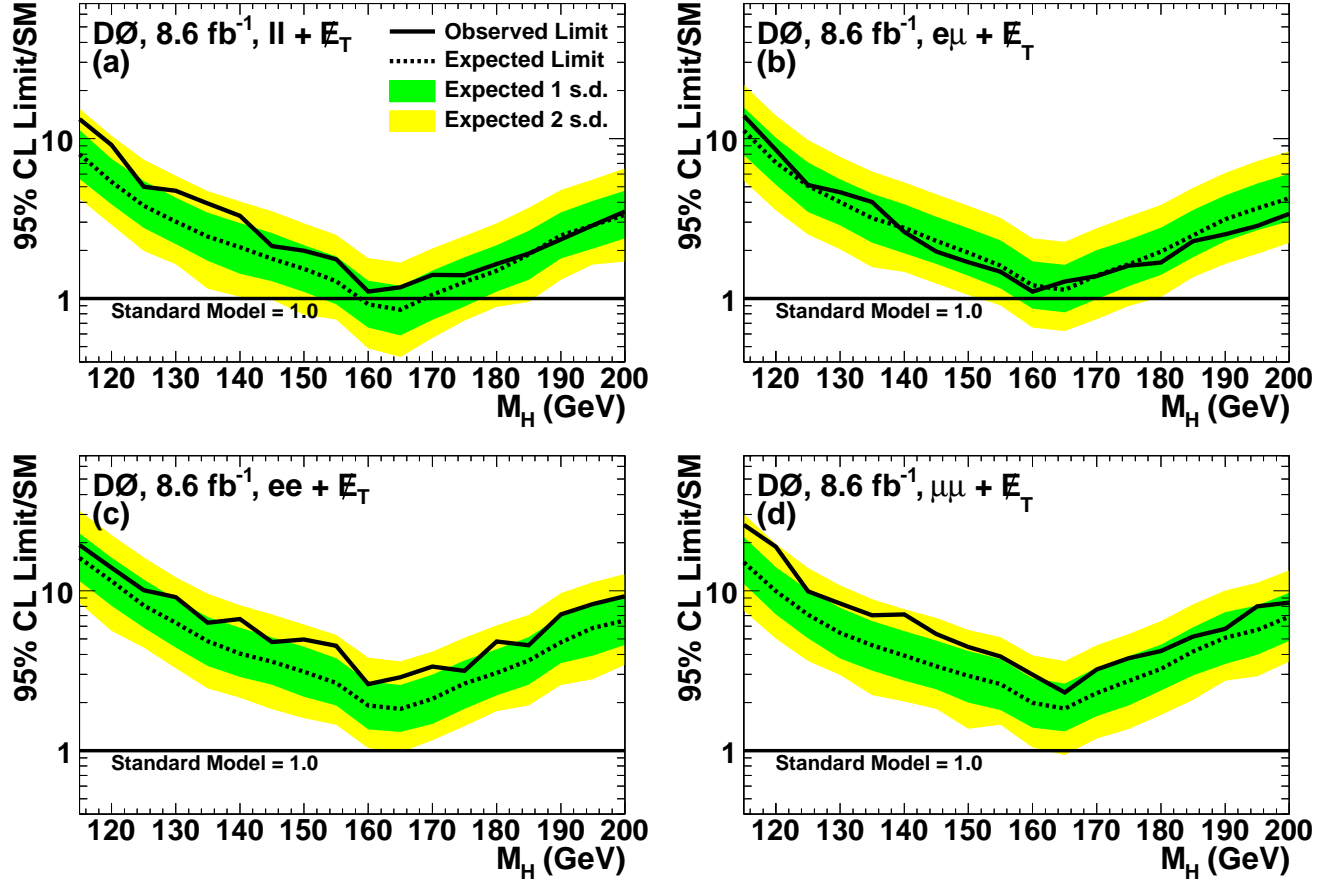


FIG. 15: [color online] Excluded cross section, $\sigma(p\bar{p} \rightarrow H + X)$, at the 95% C.L. in units of the SM cross section as a function of M_H using (a) all channels, (b) $e\mu$ channel, (c) ee channel, (d) $\mu\mu$ channel.

- Phys. Lett. B **564**, 65 (2003); Nucl. Phys. **B737**, 73 (2006).
- [23] M. L. Mangano *et al.*, J. High Energy Phys. **07**, 001 (2003); we use version 2.11.
- [24] R. Hamberg, W. L. van Neerven, and T. Matsuura, Nucl. Phys. **B359**, 343 (1991) [Erratum-ibid. **B644**, 403 (2002)].
- [25] V. M. Abazov *et al.* [D0 Collaboration], Phys. Rev. Lett. **100**, 102002 (2008).
- [26] K. Melnikov and F. Petriello, Phys. Rev. D **74**, 114017 (2006).
- [27] S. Moch and P. Uwer, Phys. Rev. D **78**, 034003 (2008); we use $\sigma(t\bar{t}) = 7.88$ pb.
- [28] J.M. Campbell and R.K. Ellis, Phys. Rev. D **60**, 113006 (1999); we use $\sigma(WW) = 11.66$ pb, $\sigma(WZ) = 3.45$ pb, and $\sigma(ZZ) = 1.37$ pb.
- [29] S. Frixione and B.R. Webber, J. High Energy Phys. **06**, 029 (2002).
- [30] R. Brun and F. Carminati, CERN Program Library Long Writup W5013, 1993 (unpublished).
- [31] M. Abolins *et al.*, Nucl. Instrum. Meth. in Phys. Res. A **584**, 75 (2008)
- [32] R. Angstadt *et al.*, Nucl. Instrum. Meth. in Phys. Res. A **622**, 298 (2010).
- [33] The pseudorapidity is defined as $\eta = -\ln[\tan(\theta/2)]$,
- where θ is the polar angle relative to the proton beam direction.
- [34] G. C. Blazey *et al.*, arXiv:hep-ex/0005012v2.
- [35] V. M. Abazov *et al.* [D0 Collaboration], Nucl. Instrum. Meth. in Phys. Res. A **620**, 490 (2010).
- [36] V. M. Abazov *et al.* [D0 Collaboration], Phys. Rev. D **85**, 052006 (2012).
- [37] J. Alwall *et al.*, Eur. Phys. J. C **53**, 473 (2008).
- [38] V. M. Abazov *et al.* [D0 Collaboration], Phys. Lett. B **669** (2008), 278.
- [39] C. G. Lester and D. J. Summers, Phys. Lett. B **463**, 99 (1999); H. Cheng and Z. Han, J. High Energy Phys. **12**, 063 (2008).
- [40] L. Breiman *et al.*, *Classification and Regression Trees* (Wadsworth, Belmont, CA, 1984); Proceedings of the Thirteenth International Conference, Bari, Italy, 1996, edited by L. Saitta (Morgan Kaufmann, San Francisco, 1996), p. 148.
- [41] I. W. Stewart and F. J. Tackmann, Phys. Rev. D **85**, 034011 (2012).
- [42] C. Anastasiou, R. Boughezal and F. Petriello, J. High Energy Phys. **04**, 003 (2009)
- [43] J. M. Campbell, R. K. Ellis, and C. Williams, Phys. Rev. D **81**, 074023 (2010).
- [44] T. Binoth, M. Ciccolini, N. Kauer, and M. Krämer, J.

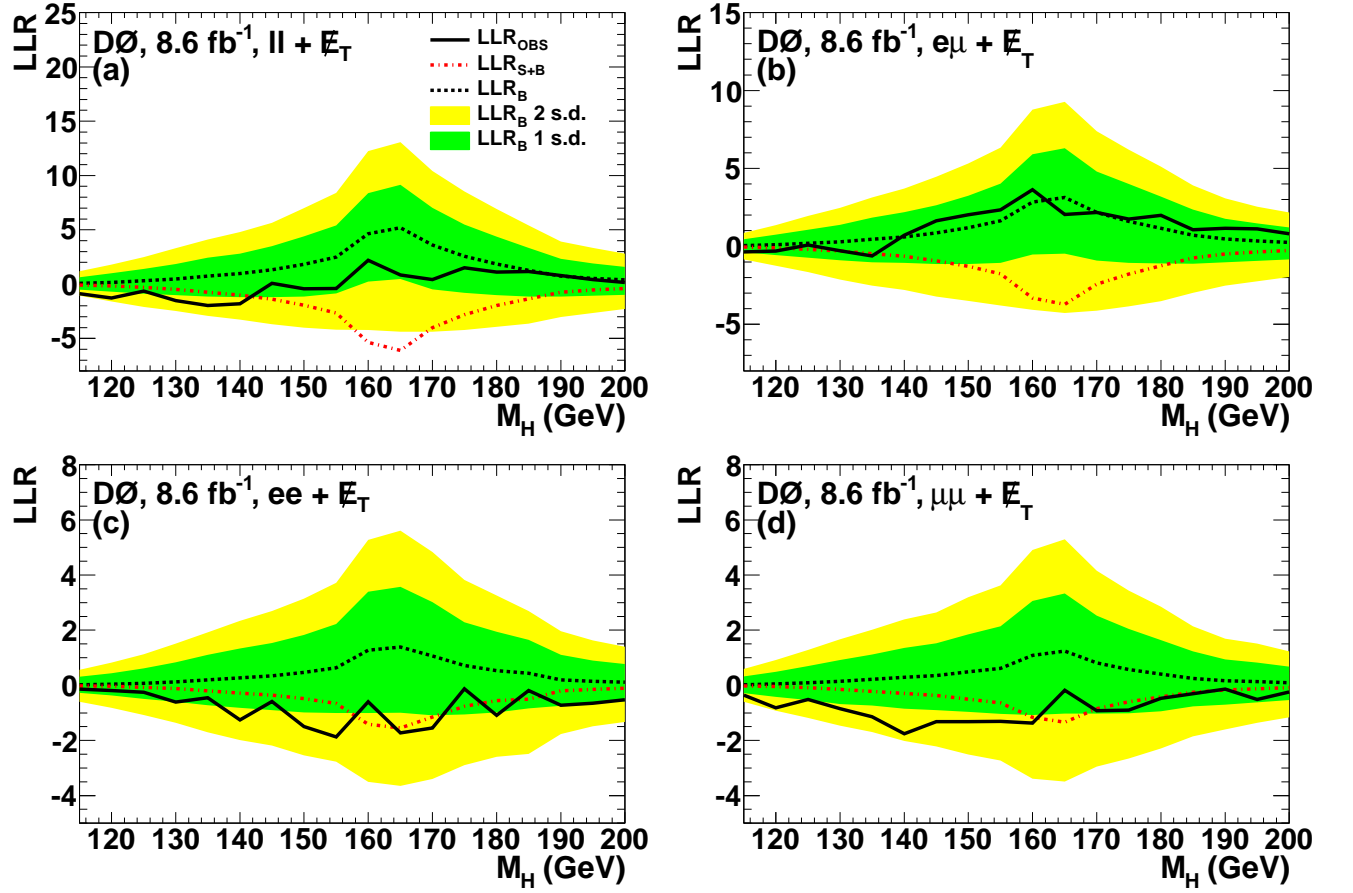


FIG. 16: [color online] The observed LLR (solid line) as a function of M_H using (a) all channels, (b) $e\mu$ channel, (c) ee channel, (d) $\mu\mu$ channel. Also shown are the expected LLR distributions for the background only hypothesis (dashed line) and for the signal+background (dash-dotted line) hypothesis, with the dark grey and light grey bands indicating ± 1 and ± 2 s.d. fluctuations of the expected LLR distributions for the background-only hypothesis, respectively.

High Energy Phys. **03**, 065 (2005); J. High Energy Phys. **12**, 046 (2006).

[45] T. Junk, Nucl. Instrum. Meth. in Phys. Res. A **434**, 435 (1999); A. Read, J. Phys. G **28**, 2693 (2002).

[46] W. Fisher, FERMILAB-TM-2386-E (2006).

[47] V. M. Abazov *et al.* [D0 Collaboration], arXiv:1207.0422 [hep-ex] (2012).